CIRRUS-HL

Picturing High-and Midlatitude Summer Cirrus and Contrail Cirrus above Europe with Airborne Measurements aboard the Research Aircraft HALO

Jurkat-Witschas, Tina; Voigt, Christiane; Groß, Silke; Kaufmann, Stefan; Sauer, Daniel; Castro, Elena De la Torre; Krämer, Martina; Schäfler, Andreas; Afchine, Armin; More Authors

DOI
10.1175/BAMS-D-23-0270.1

Publication date
2025

Document Version
Final published version

Published in
Bulletin of The American Meteorological Society

BAMS Article

CIRRUS-HL: Picturing High- and Midlatitude Summer Cirrus and Contrail Cirrus above Europe with Airborne Measurements aboard the Research Aircraft HALO

Tina Jurkat-Witschas,[a] Christiane Voigt,[a,b] Silke Groß,[a] Stefan Kaufmann,[a] Daniel Sauer,[a] Elena De la Torre Castro,[a,b,k] Martina Krämer,[b,c] Andreas Schäfler,[a] Armin Afchine,[c] Roman Attinger,[h] Irene Bartolome Garcia,[b,c] Christof G. Beer,[a] Luca Bugliaro,[a] Hans-Christian Clemen,[f] Georgios Dekoutsidis,[a] André Ehrlich,[e] Sarah Grawe,[g] Valerian Hahn,[a] Johannes Hendricks,[a] Emma Järvinen,[i] Thomas Klimach,[f] Konstantin Krüger,[f] Ovid Krüger,[f] Johannes Lucke,[a,k] Anna E. Luebke,[e] Andreas Marsing,[a] Bernhard Mayer,[d] Johanna Mayer,[a] Stephan Mertes,[g] Rubin-Zuzic Milenko,[a] Manuel Moser,[a] Hanno Müller,[e] Vladyslav Nenakhov,[m] Mira Pöhlker,[f,g] Ulrich Pöschl,[f] Veronika Pörtge,[d] Marc Rautenhaus,[l] Mattia Righi,[a] Johannes Röttenbacher,[e] Jonas Schaefer,[g] Martin Schnaiter,[i,j] Johannes Schneider,[f] Ulrich Schumann,[a] Nicole Spelten,[c] Frank Stratmann,[g] Laura Tomsche,[b] Shawn Wagner,[i] Ziming Wang,[a,b,d] Anna Weber,[d] Manfred Wendisch,[e] Heini Wernli,[h] Bruno Wetzel,[g] Martin Wirth,[a] Andreas Zahn,[i] Helmut Ziereis,[a] and Martin Zöger[m]

KEYWORDS:
Atmosphere;
Aerosols;
Cirrus clouds;
Cloud microphysics;
Water vapor;
Aircraft observations

ABSTRACT: Accurately determining and reducing the climate impact of aviation and its uncertainties is one of the pressing challenges of our times. Contrail cirrus are estimated to contribute more than half of the total effective radiative forcing from aviation, yet the uncertainties in their optical and radiative properties are large. In contrast to midlatitude cirrus, high-latitude cirrus are less anthropogenically influenced; thus, they are more pristine. However, little is known about Arctic cirrus properties and their role in the amplified warming of this region. The Cirrus in High Latitudes (CIRRUS-HL) mission using the High Altitude and Long Range Research Aircraft (HALO) provides measurements in mid- and high latitudes during summer (June/July) 2021, exploiting HALO's capabilities and a comprehensive cloud–aerosol–trace gas and radiation instrumentation. The results of 24 HALO flights provide new insights into both natural cirrus and contrail cirrus properties in high (60°–76°N) and midlatitudes (38°–60°N). In particular, we find lower ice water content (–42%) and lower number concentrations (–88%) of cirrus particles with larger mean diameters (+22%) in high latitudes. Ice supersaturated regions were frequently observed in mid- and high latitudes, with median in-cloud relative humidity over ice between 105% and 122%. Mean aerosol number concentrations in the midlatitudes were reduced by up to 80% compared

DOI: 10.1175/BAMS-D-23-0270.1
Corresponding author: Tina Jurkat-Witschas, tina.jurkat@dlr.de
Supplemental information related to this paper is available at the Journals Online website: https://doi.org/10.1175/BAMS-D-23-0270.s1.

Publisher's Note: This article was revised on 20 November 2025 to correct the affiliation of author Marc Rautenhaus.

Manuscript received 18 October 2023, in final form 21 March 2025, accepted 2 July 2025

to pre-COVID-19 times. Less air traffic during the COVID-19 lockdowns, reduced contrail cirrus coverage, and lower ice nucleating particle concentrations in high latitudes help to explain the observed differences in cirrus properties. The extensive dataset will be used to improve weather and climate models.

SIGNIFICANCE STATEMENT: In contrast to Arctic cirrus, midlatitude cirrus are more often modified by human activities, of which air traffic is a significant contributor through the formation of contrails and contrail cirrus. These man-made cirrus warm Earth, but to constrain their effects on climate, in situ and remote sensing measurements were conducted with the German research aircraft High Altitude and Long Range Research Aircraft (HALO). During 24 flights, we used HALO's exceptional altitude and distance range to sample and contrast different cirrus types from the dense air traffic regions to the remote Arctic regions. We find that microphysical properties of high- and midlatitude cirrus differ substantially, related to their formation pathway, the abundance of air traffic, and the availability of ice nucleating particles. The measurements will help to validate contrail cirrus and climate models.

AFFILIATIONS: [a] Institut für Physik der Atmosphäre, Deutsches Zentrum für Luft-und Raumfahrt, Oberpfaffenhofen, Germany; [b] Institute for Physics of the Atmosphere, Johannes Gutenberg University of Mainz, Mainz, Germany; [c] Forschungszentrum Jülich, Jülich, Germany; [d] Meteorologisches Institut, Ludwig-Maximilians-Universität München, München, Germany; [e] Leipzig Institute for Meteorology, Leipzig University, Leipzig, Germany; [f] Max Planck Institute for Chemistry, Mainz, Germany; [g] Leibniz Institute for Tropospheric Research, Leipzig, Germany; [h] Institute for Atmospheric and Climate Science, ETH Zurich, Zurich, Switzerland; [i] Karlsruhe Institute of Technologies, Karlsruhe, Germany; [j] schnaiTEC GmbH, Bruchsal, Germany; [k] Faculty of Aerospace Engineering, Delft University of Technology, Delft, Netherlands; [l] Visual Data Analysis Group, House of Computing and Data Science, Universität Hamburg, Hamburg, Germany; [m] Flugexperimente, Deutsches Zentrum für Luft-und Raumfahrt, Oberpfaffenhofen, Germany

1. Introduction and scientific background

Cirrus clouds are ice clouds that exist in the upper troposphere at temperatures below −38°C. Air masses that are lifted cool and eventually reach supersaturation, which leads to ice formation below this temperature. Cirrus clouds exert an overall net warming effect on the atmosphere–surface system, where the warming effect through absorption of thermal radiation exceeds the cooling effect through reflection of sunlight (Chen et al. 2000). The representation of cirrus clouds in general circulation models comprises a main challenge and a major uncertainty for predicting the rate and geographical pattern of climate change (Gasparini et al. 2018; Zelinka et al. 2020). Midlatitude cirrus clouds are formed in various synoptic situations with different dynamical forcings. The interplay of updraft and associated cooling with the availability of ice nucleating particles (INPs) determines whether the cirrus cloud forms homogeneously or heterogeneously (Kärcher and Lohmann 2002, 2003) and whether it forms in situ or via the liquid phase (Wernli et al. 2016; Luebke et al. 2016; Krämer et al. 2016; Voigt et al. 2017; Krämer et al. 2020). Cirrus that form at temperatures below 235 K, heterogeneously through deposition of water vapor onto preexisting INPs or homogeneously through ice nucleation in supercooled solution particles, are referred to as in situ–origin

cirrus. Liquid-origin cirrus form through the freezing of existing liquid cloud droplets, either heterogeneously at temperatures above 235 K via embedded INPs or homogeneously at 235 K. Cirrus clouds can exert a positive or a negative radiative forcing (RF) depending on a number of factors like microphysical (e.g., ice crystal size, number) and macrophysical (e.g., location, time) properties. Polar night cirrus tend to warm the atmosphere due to exclusive absorption of terrestrial radiation (Hong and Liu 2015; Marsing et al. 2023). The radiative effects of the polar-day Arctic and midlatitude cirrus depend on their optical thickness, ice crystal optical and microphysical properties, the surface albedo and emission, the vertical extension and location of the cloud, and the solar zenith angle (Krämer et al. 2020; Hong and Liu 2015; Lelli et al. 2023); thus, their effect is complicated to determine. Similar to Arctic low-level clouds and their relation to the accelerated warming of the Arctic (McFarquhar et al. 2011; Wendisch et al. 2017, 2023), the net contribution of cirrus clouds to the Arctic temperature trend is unknown. A better understanding of their influence on radiative balance (Marsing et al. 2023) and temperature in this sensitive region of Earth requires observational data of ice microphysical and optical properties, water vapor, and aerosols from the ground to the lower stratosphere, which is hard to obtain due to the limited accessibility of this region (Kay et al. 2016; Schmale et al. 2021).

Recent studies have shown that anthropogenic cirrus clouds induced by aviation (mainly contrails and the contrail cirrus that evolve from them) contribute substantially to midlatitude upper-tropospheric clouds with an expected warming effect (Minnis et al. 2004; Burkhardt and Kärcher 2011). Current aviation climate impact assessments conclude that contrail cirrus have a net effective radiative forcing with a magnitude that exceeds the effect of the integrated carbon dioxide (CO_2) emissions from aviation since the beginning of modern aviation (Lee et al. 2021). Mitigation approaches to reduce the impact of contrails include using sustainable aviation fuels (Voigt et al. 2021; Märkl et al. 2024), technological means (Gierens 2021; Bier et al. 2024), rerouting of aircraft to avoid climate-sensitive regions (Teoh et al. 2022a; Ng et al. 2024), or a combination of these measures (Teoh et al. 2022b).

A large uncertainty for the climate impact assessment of contrail cirrus is the prediction of ice supersaturated regions (ISSRs) over the lifetime of the contrail—a fundamental requirement to assess its radiative forcing (Jensen et al. 2001; Gierens et al. 2020). High-resolution (HRES) measurements of low water vapor concentrations in the upper troposphere and lower stratosphere (UTLS) have improved significantly in the past years (Thornberry et al. 2013; Rollins et al. 2014). These measurements revealed a significant model offset in current weather prediction data in the UTLS (Kaufmann et al. 2018; Krüger et al. 2022). Furthermore, uncertainties in the representation of ice crystal shape (Wendisch et al. 2005, 2007) and complexity of high- and midlatitude cirrus and contrail cirrus (Järvinen et al. 2018; Chauvigné et al. 2018), in the modification of optical properties of natural clouds through contrail cirrus (Tesche et al. 2016; Marjani et al. 2022), and in their life cycle and variability (Unterstrasser et al. 2017; Bier and Burkhardt 2022) are limiting factors to the global climate impact assessment of these man-made clouds. High-resolution upper-tropospheric measurements of water vapor and clouds are therefore key to understand the local and global effects of natural and anthropogenic cirrus (Sassen 1997; Heymsfield et al. 2017; Groß et al. 2023) and finally their climate feedback (Bock and Lauer 2024).

Here, we present an overview of the measurements performed using the High Altitude and Long Range Research Aircraft (HALO) in the frame of the Cirrus in High Latitudes (CIRRUS-HL) mission (www.cirrus-hl.de), which focused on mid- and high-latitude cirrus clouds, water vapor, and aerosols, as well as contrails and contrail cirrus during summer 2021. We provide an overview of the scope of the CIRRUS-HL campaign, the instruments, and the forecast products used for flight planning. We elaborate on the 24 flights performed between 38° and 76°N and

examine the latitudinal differences observed in the cloud, water vapor, trace gas, and aerosol data. Furthermore, selected cases are used to demonstrate the capabilities and application of the dataset by combining measurements from state-of-the-art airborne instrumentation with model data and satellite retrievals.

2. Scope of the CIRRUS-HL mission and atmospheric conditions during the campaign period

The aim of the CIRRUS-HL campaign was to probe optical, radiative, microphysical, and macrophysical properties of cirrus clouds from the midlatitude, dense air traffic regions to the high-latitude more pristine Arctic regions to investigate the following topics:

- How do the microphysical and radiative properties of cirrus clouds in Arctic regions differ from those of midlatitude cirrus clouds? Is there a distinguishable anthropogenic effect at midlatitudes? What is the relative contribution of in situ– and liquid-origin cirrus?
- Are there differences in aerosol and water vapor distributions at high and midlatitudes?
- Do contrails and contrail cirrus significantly modify microphysical, optical, and radiation properties of cirrus at midlatitudes?
- Are cirrus clouds and contrail cirrus adequately represented in climate models? What are the dominant ice nucleating particles of high- and midlatitude cirrus clouds? What is the role of cirrus clouds for the Arctic amplification?

The mission flights were conducted from Oberpfaffenhofen (southern Germany), with refueling stops in Scandinavia or Iceland for the high-latitude cirrus missions. We refer to measurements as high latitude when the aircraft was north of 60°N latitude. Sensitivity studies through variation of this latitude threshold by 5° did not substantially impact the result of the analysis (De La Torre Castro et al. 2023).

The CIRRUS-HL mission was conducted during a time when air traffic was still reduced due to the COVID-19 pandemic. According to EUROCONTROL, the number of daily flights was increasing sharply during the months of June and July 2021, but on average, it was still 65%–80% lower than in the same months of 2019. This led to reduced global contrail and contrail cirrus coverage, resulting in a 50% reduction in RF from contrail cirrus compared to pre-COVID-19 (Voigt et al. 2022; Schumann et al. 2021b,a). Thus, the CIRRUS-HL measurements were performed in a time with reduced effect of aviation on the cirrus coverage and radiative forcing.

The high-latitude cirrus flights were focused on thin cirrus clouds, with airmass origins (based on 10-day backward trajectories) in the northern latitudes (>60°N). Sea ice was at an interannual minimum during the campaign period, with less than 50% of the maximum extension in March 2021, providing cirrus measurements mainly above open ocean and above land with a high-occurrence frequency of low-level clouds. In addition, July 2021 was affected by a quasi-stationary low pressure system residing above central Europe. The enhanced heat and moisture transported from the Baltic Sea caused strong convective activity and catastrophic floods in Europe, particularly in Germany and Belgium (Lehmkuhl et al. 2022), with an unknown effect on the humidity fields at cirrus altitude (Krüger et al. 2022).

3. Overview of flights

In total, 24 flights (including 23 scientific flights and 1 test flight) were conducted between 38° and 76°N. Sampling 34 flight hours (17.7 h in midlatitude cirrus, 7.8 h in high-latitude cirrus, and the remaining time in mixed-phase and liquid clouds) provided in situ measurements at temperatures down to −63°C and altitudes up to 14.3 km. A list of the research objectives of the individual flights, and the altitude, geographical, and temperature ranges sampled, is

presented in Table 1. An overview of the horizontal and vertical flight paths of the individual flights is presented in Fig. 1 and the movie in the online supplemental material. We also provide an overview on the number of measurements in liquid-origin and in situ cirrus per 2°-latitude band. The classification of these cirrus types is based on liquid water content (LWC) and ice water content (IWC) predicted by the European Centre for Medium-Range Weather Forecasts (ECMWF) data along 10-day backward trajectories calculated with Lagrangian Analysis Tool (LAGRANTO) (Sprenger and Wernli 2015). Starting from the HALO flight paths, the hourly backward evolution of the IWC and LWC along the trajectories was evaluated to estimate the age of the cloud and distinguish between in situ– and liquid-origin cirrus. If liquid water was present along the trajectory between cloud formation and the measurement point, we refer to the cloud as a liquid-origin cirrus following the approach described in Wernli et al. (2016) and Luebke et al. (2016) and for CIRRUS-HL data explained in more detail in De La Torre Castro et al. (2023).

Table 1. Summary of the CIRRUS-HL science flights in June and July 2021 including objectives, flight times, in-cloud and clear-sky sampling times (below 235 K), latitude, and longitude ranges. Measurement altitude and temperature ranges are indicated only for the cirrus regime measurements. For flights with targets above ground-based stations like TROPOS in Leipzig, MIM, and HP, ground-based radar or lidar data are available.

Flight	Date	Flight duration	In-cloud/ clear sky	Latitude (°N)	Longitude (°W)	Altitude (km)	Temperature (°C)	Targets
F02	25 Jun 2021	5 h 48 min	42 min/ 3 h 55 min	[43.6, 54.3]	(6.0, 13.4)	[8.5, 9.8]	[–49.5, –38]	ML cirrus above Germany, embedded contrails (section 7c)
F03	26 Jun 2021	7 h 28 min	1 h 40 min/ 4 h 12 min	[43.1, 52.4]	(0.5, 12.5)	[8.8, 11.4]	[–56, –38]	ML cirrus, embedded contrails, overpass Leipzig, MIM/HP
F04	28 Jun 2021	7 h 34 min	2 h 5 min/ 3 h 46 min	[43.7, 53.7]	(6.0, 13.3)	[9.2, 12.2]	[–60.9, –38]	ML frontal cirrus, embedded contrails, overpass Leipzig, MIM/HP
F05/F06	29 Jun 2021	10 h 43 min	3 h 15 min/ 5 h 25 min	[47.8, 71.1]	[–17.5, 13.6]	[9.2, 12.5]	[–62.7, –38]	HL (Iceland and Norway) and ML cirrus, embedded contrails; overpass MIM/HP
F07	1 Jul 2021	5 h 7 min	1 h 1 min/ 2 h 5 min	[47.6, 53.4]	(7.8, 20.7)	[8.7, 11.3]	[–55.9, –38]	ML cirrus, embedded contrails
F08/F09	5 Jul 2021	11 h 22 min	2 h 21 min/ 7 h 21 min	[48.0, 75.6]	(0.1, 22.0)	[9.2, 11.6]	[–57, –39.6]	HL cirrus (Norway)
F10/F11	7 Jul 2021	11 h 5 min	1 h 17 min/ 8 h 13 min	[47.9, 67.7]	[–29.8, 11.4]	[10, 13.8]	[–54.3, –44.2]	HL cirrus (Iceland), contrails, BB (section 8)
F12	8 Jul 2021	4 h 51 min	1 h 33 min/ 1 h 53 min	[45.3, 49.1]	(8.4, 13.2)	[9, 11.7]	[–53.2, –38]	ML cirrus, convection over the Alps (supplemental material)
F13/F14	12 Jul 2021	11 h 16 min	3 h 18 min/ 5 h 47 min	[47.7, 67.0]	[–24.4, 11.6]	[8.8, 11.7]	[–55.1, –38]	HL and ML cirrus, contrails (section 5)
F15	13 Jul 2021	5 h 15 min	1 h 30 / 1 h 44 min	[44.6, 49.9]	(9.5, 12.9)	[9.5, 12]	[–53.8, –38]	ML cirrus, convection, dust
F16/F17	15 Jul 2021	10 h 23 min	1 h 31 min/ 6 h 16 min	[38.2, 48.2]	[–8.7, 11.7]	[8.7, 14.3]	[–61.6, –38]	In situ–origin ML cirrus, contrail outbreak
F18/F19	19 Jul 2021	10 h 49 min	1 h 31 min/ 6 h 3 min	[48.1, 63.4]	[–10.4, 11.4]	[9.1, 11.8]	[–60, –38]	HL cirrus, contrails, soot cirrus
F20/F21	21 Jul 2021	10 h 9 min	1 h/7 h 28 min	[42.0, 49.0]	[–8.4, 11.4]	[9.9, 13.6]	[–56.4, –41.1]	In situ–origin ML cirrus, contrails, *CALIPSO* overpass (section 7c)
F22	23 Jul 2021	8 h 2 min	1 h 3 min/ 5 h 51 min	[48.1, 61.1]	[–5.7, 11.4]	[9.2, 11.5]	[–57.2, –38]	HL cirrus, day–night, embedded contrails
F23	28 Jul 2021	6 h 49 min	41 min/ 3 h 49 min	[48.0, 64.3]	[–8.2, 11.4]	[7.5, 11.9]	[–52.9, –38]	HL cirrus and ML, *CALIPSO* overpass
F24	29 Jul 2021	4 h 16 min	–/2 h 27 min	[48.0, 51.8]	[8.3, 13.1]	—	—	Nose boom turbulence calibration

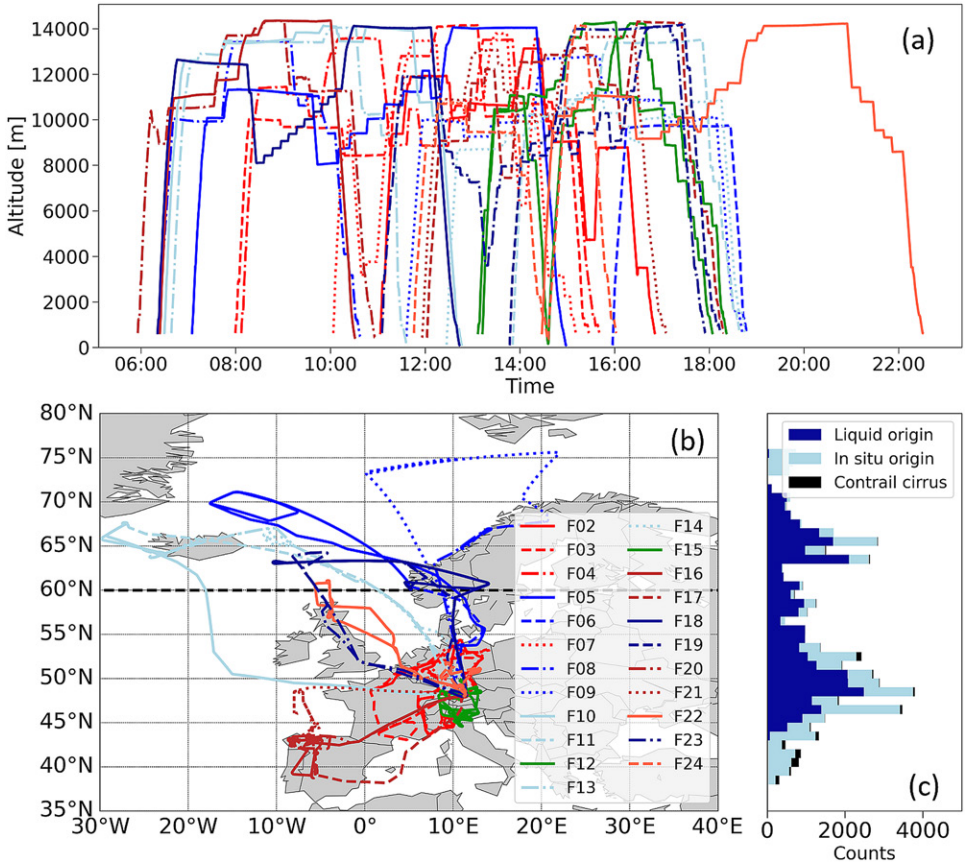

Fig. 1. Overview of region, time, and altitude of CIRRUS-HL scientific flights. (a) GPS altitude profile of 23 CIRRUS-HL flights with respect to the time of the day (UTC). High-altitude flight legs were dedicated to remote sensing measurements. Cirrus were probed in situ with a staircase flight pattern ascending through the clouds. (b) Map with flight paths of 23 flights. Flights at high latitudes are indicated with blue colors, red colors represent flights at midlatitudes, and green colors indicate flights in convection. The 60° of latitude is indicated with a thick dashed line. (c) Number of cloud encounters classified as either liquid-origin, in situ–origin, or contrail cirrus per 2°-latitude interval. Contrail cirrus were mainly found above continental Europe.

Next to thin jet stream cirrus, liquid-origin cirrus in high and midlatitudes were sampled, contrail cirrus cluster, day-and-nighttime radiative effects of cirrus, and cirrus formed on aviation soot were investigated, and dedicated measurements of cloud vertical profiles in convective cirrus were performed (see supplemental material). With the exception of two flights focusing on convective cirrus, mostly synoptically forced cirrus were targeted. Cirrus and mixed-phase clouds were also targeted above ground-based observational sites like the radar station of the German Weather Service in Hohenpeißenberg (HP) and the lidars and ceilometers at the Leibniz Institute for Troposphärenforschung (TROPOS) institute in Leipzig and the Meteorological Institute Munich (MIM).

Contrail cirrus were detected in situ as isolated clusters, above cirrus, and embedded in cirrus, with collocated remote sensing measurements (see section 7c). In total, more than 600 contrail cirrus encounters with contrail ages between 100 and 10 000 s were detected in situ during the campaign. Based on this analysis, a contrail cirrus flag was derived that identifies sequences of individual contrail cirrus encounters using coincident measurements of nitric oxide (NO) and aerosol number in the dataset. A class of contrail cirrus with high ice crystal number ($N_{ice} > 0.1$ cm^{-3}) and low effective diameter (ED < 40 μm) was identified in the in situ data (De La Torre Castro et al. 2023). We discuss the effect of contrail cirrus on upper-tropospheric humidity in section 6c and on radiation in section 7d. An overview of the cloud microphysical properties is given in section 6.

So-called missed approach flight patterns were repeatedly performed above European cities during the campaign to randomly capture the aerosol, cloud, and trace gas vertical profiles in dense air traffic and remote regions. These vertical profiles provide information on the aerosol background during the campaign for comparisons with models, i.e., ECHAM/Modular Earth Submodel System (MESSy) Atmospheric Chemistry (EMAC; Kaiser et al. 2019; Beer et al. 2020; Righi et al. 2020) and MECO(n) (Mertens et al. 2016), and relate atmospheric conditions to previous aerosol and trace gas conditions in pre-COVID-19 and lockdown conditions, e.g., during BLUESKY (Voigt et al. 2022; Tomsche et al. 2022) (see section 6b).

4. HALO instrumentation

The HALO instrumentation for CIRRUS-HL is based on the payload of the previous in situ cloud mission Midlatitude CIRRUS (ML-CIRRUS) (Tables 1 and 2 in Voigt et al. 2017). It comprised a comprehensive and extended payload to characterize ice particle residuals (IPRs), aerosol size, number and composition, INP concentration, cirrus ice crystal microphysical and optical properties, radiative fluxes, and humidity in the tropopause region. A list of cabin-based instruments and underwing cloud probes with the measured quantity, respective size range, and acronym is given in Tables 2 and 3.

Figure 2 provides pictures of instruments central to this study and of new instruments deployed for the first time on HALO. One significant improvement to the previous mission is the new mounting position of the counterflow virtual impactor (Ogren et al. 1985) for HALO (HALO-CVI) at the lower fuselage (Fig. 2a), as cloud particle enrichment and shadow effects are significantly lower compared to sampling at the upper fuselage. This cloud inlet sampled cirrus ice particles and provided their IPR to a number of aerosol instruments. This mainly includes two ultrahigh sensitivity aerosol spectrometers [CVI-ultrahigh sensitivity aerosol spectrometer (UHSAS) and fast aerosol size distribution (FASD)-UHSAS; Cai et al. 2008], the single-particle laser ablation mass spectrometer Aircraft-Based Laser Ablation Aerosol Mass Spectrometer (ALABAMA) (Brands et al. 2011; Clemen et al. 2020), the Soot Particle Mass and Absorption Measurement System (SOPAMA) system including a single-particle soot photometer extended range (SP2xr; Droplet Measurement Technologies) instrument, two tricolor absorption photometers (TAPs; Brechtel Inc), and the sampler High Volume Aerosol

Table 2. Underwing cloud probes deployed on HALO during CIRRUS-HL.

Instruments	Measured properties, range	PI, institution	Reference
Cloud Combination Probe (CCP)	Cloud particle size distribution, 2–960 μm	Voigt, University of Mainz	De La Torre Castro et al. (2023)
Precipitation Imaging Probe (PIP)	Cloud particle size distribution, 100–6400 μm	Voigt, University of Mainz	De La Torre Castro et al. (2023)
Novel Ice Experiment–Cloud and Aerosol Particle Spectrometer (NIXE-CAPS)	Cloud particle size distribution, 0.5–960 μm	Krämer, FZJ	Krämer et al. (2020)
Small Ice Detector Mark 3 (SID-3)	Ice particle size and phase, 2–50 μm	Schnaiter, KIT	Vochezer et al. (2016)
Particle Habit Imaging and Polar Scattering Probe (PHIPS)	Ice particle habit and phase function, 10–1000 μm	Järvinen, KIT	Schnaiter (2016)
Cloud and Aerosol Spectrometer with Depolarization Detection (CAS-DPOL)	Ice particle size distribution, 0.5–50 μm	Jurkat-Witschas, Voigt, DLR	Voigt et al. (2021)
Passive Cavity Aerosol Spectrometer Probe (PCASP-100X)	Dry particle size distribution, 0.12–3, 5 μm	Sauer, DLR	Voigt et al. (2022)
Microwave Temperature Profiler (MTP)	Temperature profiles	Tomsche, DLR	Heckl et al. (2021)

Table 3. Cabin-based instruments deployed on HALO during CIRRUS-HL.

Instruments	Measured properties, range	PI, institution	Reference
WALES high spectral resolution lidar with H_2O differential absorption channel	Water vapor concentrations, backscatter ratio, and polarization	Wirth, DLR	Wirth et al. (2009)
Albedometer for Spectral Modular Airborne Radiation Measurement System (SMART)	Spectral radiance, spectral irradiance (350–2200 nm)	Wendisch, University of Leipzig	Ehrlich et al. (2008)
Broadband Aircraft Radiometer Instrumentation (BACARDI)	Upward and downward solar (0.3–3 μm) and thermal infrared (3–100 μm) irradiances	Giez, Wendisch, DLR, University of Leipzig	Ehrlich et al. (2023)
HALO–counterflow virtual impactor system (HALO-CVI) inlet with CPC/UHSAS/ PSAP/WVSS-II	Cloud particle residual number concentration, size distribution (0.65 nm–1 μm), absorption coefficient, IWC	Mertes, TROPOS	Cai et al. (2008), Mertes et al. (2004), Vance et al. (2015)
High-Volume Flow Aerosol Particle Filter Sampler (HERA)	Aerosol particle sampling for offline immersion INP analysis between 0° and –30°C freezing temperature	Stratmann, TROPOS	Grawe et al. (2023)
Aerosol Measurement System with condensation particle counter (CPC)/ optical particle counter (OPC)/ differential mobility analyzer (DMA)/AMETYST	Size distribution of total and nonvolatile aerosol (4–2 μm), absorption	Sauer, DLR	Voigt et al. (2017)
Ultrahigh sensitivity aerosol spectrometer (UHSAS)	Number size distribution of aerosol particles in a size range from 60 to 1000 nm	Pöhlker, Pöschl, MPIC	Andreae et al. (2018), Mei et al. (2020)
Aircraft-Based Laser Ablation Aerosol Mass Spectrometer (ALABAMA)	Chemical composition of aerosol/cloud residual ($\gtrsim$ 200 nm)	Schneider, MPI-C	Brands et al. (2011), Clemen et al. (2020)
Soot Particle Mass and Absorption Measurement System (SOPAMA)	rBC single-particle masses and bulk aerosol absorption coefficients at 3 wavelengths	Sauer, DLR	
Backscatter Cloud Probe with Depolarization (BCPD)	Cloud particles (2–42 μm), aspherical fraction	Jurkat-Witschas, Lucke, DLR	Lucke et al. (2023)
Spectrometer of the Munich Aerosol Cloud Scanner (specMACS)	Spectral radiance (400–2500 nm, 32.7°–35.5° field of view), Stokes vectors (91° × 117° field of view, RGB color channels)	Mayer, LMU	Ewald et al. (2016), Weber et al. (2024)
Airborne H_2O Mass Spectrometer (AIMS)	H_2O, 0.1–400 ppmv	Kaufmann, DLR	Kaufmann (2016)
Lyman-alpha fluorescence hygrometer (FISH)	H_2O, total water, or gas-phase water, 1–1000 ppmv	Krämer, FZJ	Krämer (2009)
Sophisticated Hygrometer for Atmospheric Research (SHARC)	Tunable diode laser hygrometer, gas-phase water vapor, 2–40 000 ppmv	Zöger, DLR	Kaufmann et al. (2018)
Water Vapor Analyzer (WARAN)	Tunable diode laser hygrometer, total water, or gas-phase water, 1–40 000 ppmv	Marsing, Voigt, DLR	Voigt et al. (2017), Marsing et al. (2023)
Fast Airborne Ozone Instrument (FAIRO)	O_3, mixing ratio	Zahn, KIT	Zahn et al. (2012)
Atmospheric Nitrogen Oxides Measuring System (AENEAS)	NO, NO_2, 10 pptv–60 ppbv	Ziereis, DLR	Ziereis et al. (2022)
Basic HALO Measurement and Sensor System (BAHAMAS)	T, p, u, υ, meteorological and aircraft state parameters	Giez, DLR	Giez et al. (2021)

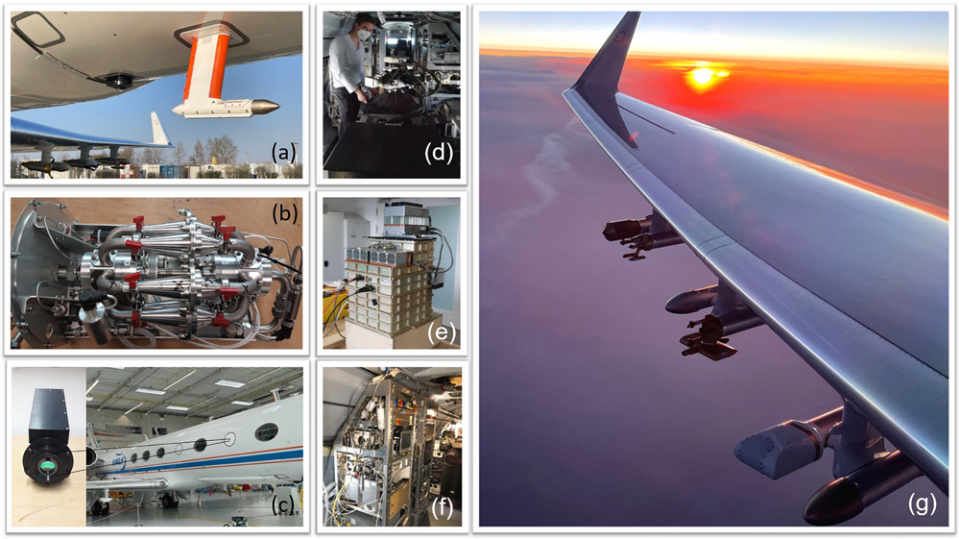

Fig. 2. Selected instruments (newly) deployed on HALO during CIRRUS-HL: (a) CVI mounted at the lower fuselage next to BACARDI. In the background, the wingpods for the PIP, SID-3, and CAS-DPOL are visible. (b) Picture of the HERA4HALO sampler. (c) Picture of the BCPD and mounting position on HALO at the second window on the right. (d) Picture of the cabin with the HSRL lidar WALES. (e) Picture of the specMACS camera system. (f) HALO rack with aerosol and the trace gas instrumentation (SP2xr, TAP, UHSAS, and Picarro). (g) Picture of the right wing carrying (from outside position to inside) the PHIPS, the CCP, the NIXE-CAPS, and the MTP during cirrus and contrail sampling at sunset. Acronyms are explained in Tables 2 and 3.

Sampler for HALO (HERA4HALO) (Grawe et al. 2023). Most of the aerosol instruments connected to the HALO-CVI were alternating and also operated behind the HALO Submicrometer Aerosol Inlet (HASI). Interstitial aerosol measurements were affected by cloud hydrometeors, and therefore, aerosol measurements with the HASI inlet were only used in cloud-free conditions. Figure 2b shows the HERA4HALO sampler, deployed for the first time on HALO during CIRRUS-HL. The sampler allows for up to six filters being selectively sampled during one research flight. After the flight, filters were removed from their holders and kept frozen in a freezer at −20°C until used for offline immersion INP measurements (see, e.g., Grawe et al. 2023). Figure 2c shows the Backscatter Cloud Probe with Depolarization (BCPD) installed on the second window on the right side of the aircraft. The BCPD detects particles in the size range between 2 and 42 μm through light scattering in the 155° backward direction (Lucke et al. 2023). The BCPD was deployed on HALO for the first time for comparison to underwing cloud probes. Backscatter lidar and water vapor differential absorption lidar (DIAL) profiles were recorded using the airborne demonstrator for the Water Vapor Lidar Experiment in Space (WALES) (Wirth et al. 2009; Groß et al. 2014) (see Fig. 2d). The dataset gives time series of vertical profiles of backscatter ratio, particle depolarization, and water vapor molecular density measured along the flight path of HALO. Backscatter ratio and aerosol depolarization data are given with 1-s time resolution and 15-m vertical resolution at a wavelength of 532 nm. The backscatter profiles are extinction corrected using the high spectral resolution lidar (HSRL) method (Esselborn et al. 2008). The water vapor profiles have a time resolution of 12 s and a vertical binning of 15 m. As the DIAL measures the molecular density of water vapor, temperature/pressure data have to be used to convert this into mixing ratio or relative humidity. For this purpose, ECMWF analyses are interpolated in space and time to the lidar curtain.

A new element of the CIRRUS-HL payload was the Spectrometer of the Munich Aerosol Cloud Scanner (specMACS; Ewald et al. 2016; Weber et al. 2024) shown in Fig. 2e. It is a high-spatial-resolution hyperspectral and polarized imaging system and operates in a downward-looking perspective. The instrument consists of two hyperspectral cameras with a field of view of

32.7° and 35.5°, respectively, which are sensitive to the wavelength range between 400 and 2500 nm. In addition, the spectrometers are complemented by two 2D red–green–blue (RGB) polarization-resolving cameras with a maximum combined field of view of 91° ×117°. The radiative energy budget at flight altitude was measured with the Broadband Aircraft Radiometer Instrumentation (BACARDI; Ehrlich et al. 2023) and the Spectral Modular Airborne Radiation Measurement System (SMART; Wolf et al. 2019). BACARDI consists of two sets of pyranometers and pyrgeometers to cover the upward and downward solar (0.3–3 μm) and thermal infrared (3–100 μm) irradiances. This combination allows net irradiances to be quantified and with the help of radiative transfer simulations to calculate the cloud-radiative effect as described by Luebke et al. (2022). Spectrally resolved solar irradiances (upward and downward) are measured by SMART in the wavelength range between 0.3 and 2.1 μm (2–10 nm spectral resolution). In addition, a suite of trace gas measurements including ozone (O_3) from the Fast Airborne Ozone Instrument (FAIRO) (Zahn et al. 2012), nitrogen oxide, and the sum of reactive nitrogen (NO and NO_y) from the Atmospheric Nitrogen Oxides Measuring System (AENEAS) instrument (Ziereis et al. 2022) together with CO_2 and methane (CH_4) measured with a Picarro instrument (Klausner 2020) provided important information on the tropospheric and stratospheric airmass composition. Water vapor was measured using several in situ instruments: the Fast In Situ Stratospheric Hygrometer (FISH) (Schiller et al. 2008; Meyer et al. 2015), the Airborne H_2O Mass Spectrometer (AIMS) (Kaufmann 2016; Jurkat et al. 2016), the Sophisticated Hygrometer for Atmospheric Research (SHARC) (Kaufmann et al. 2018), and the Water Vapor Analyzer (WARAN) instrument (Marsing et al. 2023). The measurement capabilities of these instruments are documented in Kaufmann et al. (2018).

5. Forecast products and flight planning

A set of tailored forecast products was developed for CIRRUS-HL with the aim to visualize predictions of natural and aircraft-induced cirrus occurrence and their thermodynamic environment, to estimate cirrus properties in relation to distinct formation pathways, and to support flight planning. To illustrate the range of utilized flight planning tools, Fig. 3 shows selected products for planning the flight on 12 July 2021. The flight planning process involved the analysis of routinely produced charts at different pressure levels and forecast lead times. The detailed elaboration of flight plans was supported by interactive visualizations (Figs. 3a,b) using the Mission Support System (MSS; Rautenhaus et al. 2012; Bauer et al. 2022), e.g., to create vertical sections showing ECMWF forecast data along planned flight tracks. Figure 3a gives an overview of the synoptic situation and the cirrus regions at different latitudes covered by the flight from Oberpfaffenhofen to Iceland. As dedicated cloud-type sampling was pursued and different cloud formation processes were investigated, we employed the Lagrangian microphysics model CLaMS-Ice, which calculates detailed cirrus microphysical properties along 3D trajectories from ECMWF by means of a two-moment ice microphysics scheme (Luebke et al. 2016; Baumgartner et al. 2022). CLaMS-Ice products are IWC (see Fig. 3b), ice crystal number concentration N_{ice}, ice crystal mean mass size R_{ice}, origin classification of cirrus (liquid or in situ), and the identification of the ice nucleation mechanism (heterogeneous or homogeneous).

Related to a low pressure system west of Norway, an in situ cirrus (light blue) region was predicted east of Iceland (Figs. 3a,e). An additional band of mostly liquid-origin cirrus (dark blue) over Iceland was also predicted by backward trajectories using the offline tool (LAGRANTO; Wernli and Davies 1997; Sprenger and Wernli 2015) and wind fields from ECMWF forecasts (Fig. 3d). Contrail optical thickness (Fig. 3c), calculated by the Contrail and Cirrus Prediction Tool (CoCiP) model (Schumann 2012) with air traffic data from previous years, predicted contrail clusters embedded in cirrus over Germany and north of England. In addition to the classic 2D forecast products, the interactive visual analysis

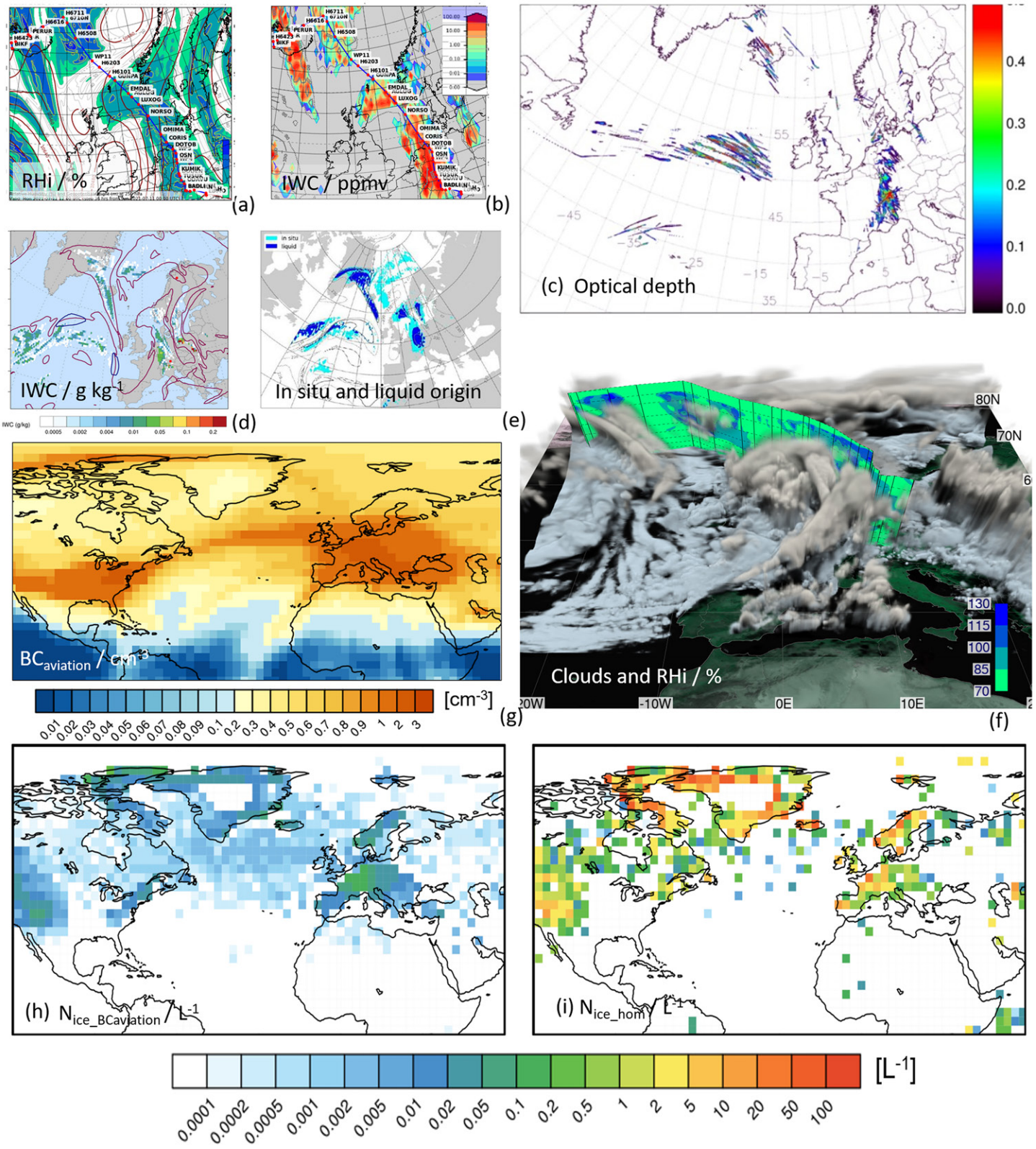

Fig. 3. Selected forecast products used for the planning of the flight on 12 Jul 2021: (a) MSS plot showing the planned flight track on top of RHi (color; %) and geopotential height (contours; m) at 250 hPa of the ECMWF HRES forecast from 0000 UTC 12 Jul 2021, valid at 1200 UTC 12 Jul 2021, (b) forecast of IWC from CLaMS-Ice trajectories (color; ppmv), (c) CoCiP forecast of contrail optical thickness (color), (d) forecast of IWC of liquid-origin cirrus based on LAGRANTO trajectories (color; g kg^{-1}), (e) forecast of liquid-origin (light blue) and in situ (dark blue) cirrus from CLaMS-Ice, (f) Met.3D volumetric visualization of forecast clouds, together with a vertical section along the flight track showing RHi [same color bar as in (a)], and climatological distributions in June and July at 260 hPa from the global model EMAC with MADE3 microphysics of (g) black carbon number concentrations from aviation and of number concentrations of ice crystals nucleated via (h) heterogeneous freezing on aviation soot particles and (i) homogeneous freezing.

software "Met.3D" (Rautenhaus et al. 2015; Schäfler and Rautenhaus 2023) was used for rapid 3D exploration of available forecast data [as done before, e.g., during the North Atlantic Waveguide and Downstream Impact Experiment (NAWDEX) campaign (Schäfler et al. 2018)]. 3D visualizations included displays of forecast cloud fields (Fig. 3f); a detailed description of our experiences using 3D visualization during CIRRUS-HL was described by Schäfler and Rautenhaus (2023).

In preparation for the campaign, we also applied the global aerosol–climate model EMAC model (Jöckel et al. 2010) including the MESSy aerosol microphysics submodel Modal Aerosol Dynamics Model for Europe, Adapted for Global Applications, Third Generation (MADE3; Kaiser et al. 2014, 2019; Beer et al. 2020), coupled to (cirrus) clouds via a two-moment cloud scheme (Kuebbeler et al. 2014; Righi et al. 2020). The simulation data used for the flight planning are based on the experiments BASE and S14F01 of Righi et al. (2021). Climatological means were calculated from the 15-yr (2001–15) simulations to characterize the atmospheric distribution of potential INPs (e.g., aviation soot) and of ice crystals nucleated via heterogeneous and homogeneous freezing, to identify regions where INP–cirrus interactions could potentially be observed during the campaign. Figure 3g shows the model climatological distribution of aviation soot particle number concentration in the upper troposphere in summer, while Figs. 3h and 3i depict upper-tropospheric number concentrations of ice crystals nucleated via heterogeneous freezing on aviation soot particles and via homogeneous freezing, respectively. The climatological distributions were used during flight planning to target cirrus regions potentially affected by aviation emissions and homogeneous nucleation. In a separate study, we will compare the measured occurrence and properties of aerosol and cirrus clouds with the model climatology to assess representativity.

6. Overview of cloud, aerosol, and trace gas distribution during CIRRUS-HL

In this section, we present an overview of ice microphysical properties, trace gases, and aerosol distributions measured during CIRRUS-HL focusing on the contrast between mid- and high latitudes in June and July 2021.

a. Microphysical properties of cirrus at mid- and high latitudes. One of the central aims of CIRRUS-HL was to investigate and contrast mid- and high-latitude microphysical cirrus properties. We here report on two datasets from two different combination probes, the Cloud Combination Probe (CCP) mounted on the outbound right-wing position and the Novel Ice Experiment–Cloud and Aerosol Particle Spectrometer (NIXE-CAPS) mounted on the central left-wing position. The occurrence frequencies of IWC, ice crystal number concentration N_{ice}, and size (mean mass radius R_{ice} or ED) are shown in Fig. 4. In addition, the median and the 10th and 90th percentiles of the climatology from Krämer et al. (2020) for 1-K temperature bins are given. A summary of the microphysical properties of cirrus clouds from all flights from the CCP is given in Figs. 4a–c, while the data from the NIXE-CAPS separated for mid- and high latitudes are shown in Figs. 4d–f and 4g–i, respectively. In general, the probes showed a good agreement throughout the mission. The IWC (Fig. 4a) increases with increasing temperature, while N_{ice} (Fig. 4b) has no clear trend, since the increase in IWC is caused by larger ice particles [see (Fig. 4c), ED] that have grown due to a higher amount of available water vapor in the warmer part of the cirrus temperature range. To get an impression of the types of cirrus observed in high and midlatitudes over Europe during CIRRUS-HL, we examine the IWC in more detail (Figs. 4a,d,g) relative to the median, the core minimum, and the core maximum IWC from Schiller et al. (2008). According to the study (liquid-origin cirrus; Krämer et al. 2016), combining cirrus simulations with observed climatologies, IWCs above the median and even above the core maximum line originate from glaciated mixed-phase

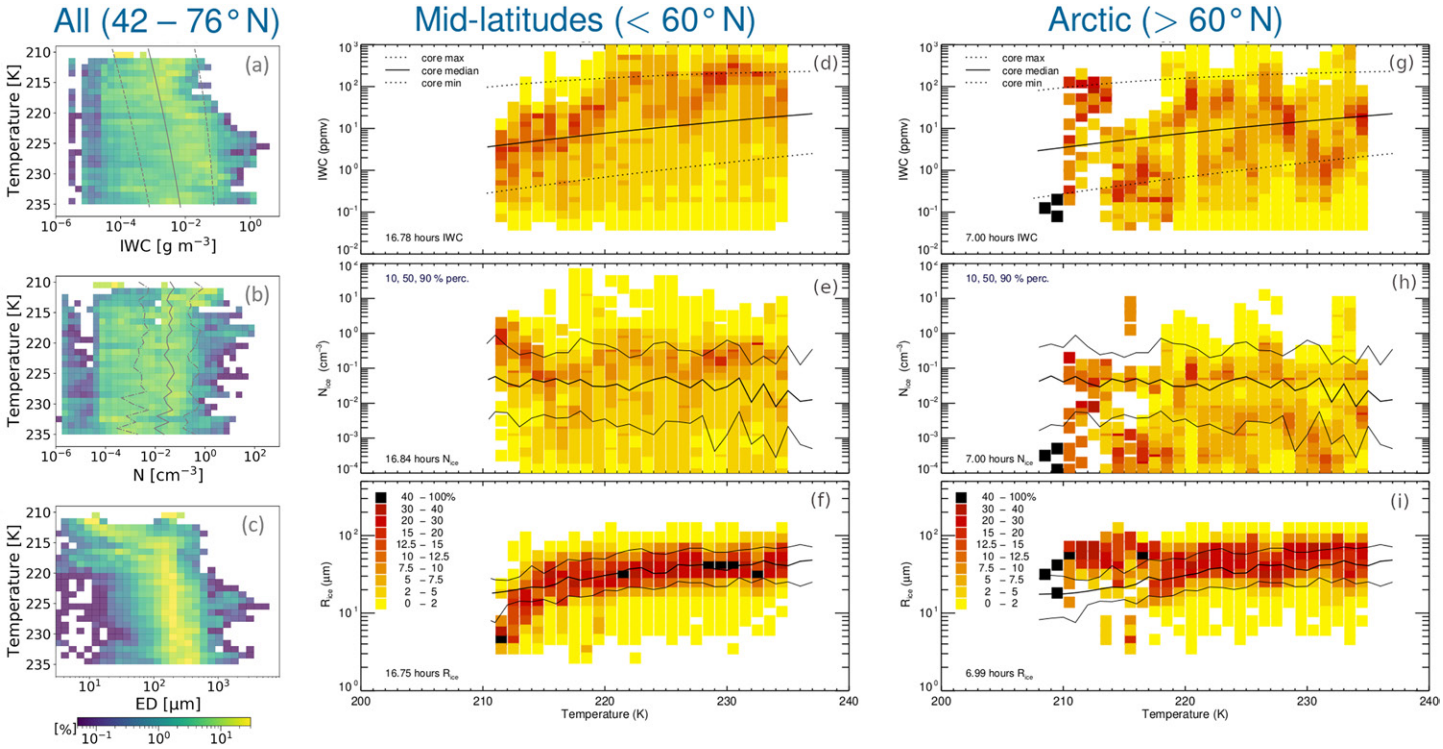

Fig. 4. Frequencies of occurrence of the cirrus microphysical properties (IWC, N_{ice}, ED, and R_{ice}) with respect to temperature. (a)–(c) All measurements 38°–76°N (from CCP + PIP; De La Torre Castro et al. 2023); (d)–(f),(g)–(i) midlatitude (>60°N) and Arctic (<60°N) measurements (from NIXE-CAPS; Krämer et al. 2016). IWC: calculated from the ice particle size distributions by using the mass-dimension relation shown in Krämer et al. (2016) and Afchine et al. (2018); N_{ice}: ice crystal number concentration; R_{ice}: ice crystal mean mass radius (~IWC/N_{ice}); ED: ice crystal effective diameter; IWC lines: minimum, median, and maximum of the IWC core range from Schiller et al. (2008); N_{ice} and R_{ice} lines: 10th, 50th, and 90th percentiles from Krämer et al. (2020).

clouds formed at lower altitudes that are uplifted in strong convective updrafts over a great vertical distance and thus carry a large amount of frozen water. Vertical velocities were measured by HALO. In addition, updraft speeds along the backward trajectories were analyzed. Under these atmospheric conditions of high updraft velocities, which were encountered twice during dedicated convective flight above the Alps (Schäfler and Rautenhaus 2023), the IWCs reached values up to ≈3 g m^{-3} (≈2000 ppmv; see also supplemental material) that also led to aircraft pitot icing (Kalinka et al. 2023).

These thick cirrus occurred mainly in midlatitudes at higher temperatures and lower altitudes ($\gtrsim 220\,\mathrm{K}$, $\lesssim 10\,\mathrm{km}$; Fig. 4d). Based on classification from Krämer et al. (2016, 2020), observations between the median and the core maximum IWC can be assigned to liquid-origin cirrus in frontal systems, where the updrafts are less intense than those in convective cirrus. Using this classification, approximately half of the cirrus probed in midlatitudes during CIRRUS-HL were liquid-origin cirrus (see Fig. 1 and De La Torre Castro et al. 2023). The thinner cirrus with low IWCs mostly appeared on top of frontal systems or in high pressure systems. The term N_{ice} shows overall occurrence frequencies slightly above the median in the midlatitudes (Fig. 4e), indicating contrail cirrus or cirrus formed in high updrafts. The occurrence frequencies of midlatitude ice crystal sizes R_{ice} are shown in Fig. 4f. The smallest R_{ice} have been observed together with the highest N_{ice} around 212–216 K. These observations can be traced back to young contrails and contrail cirrus using coincident measurements of nitrogen oxides and nonvolatile particulate matter.

In the Arctic, greater variability is observed in the cirrus IWC compared to the midlatitude cirrus (Fig. 4g). Based on backward-trajectory analysis, 30% thin in situ cirrus with low IWC and 70% thick liquid-origin cirrus with higher IWC, mostly advected from the midlatitudes into the Arctic, were probed. This indicates a significant influence of midlatitude air on the

Arctic cirrus composition. The enhanced frequencies of very low IWCs ($\lesssim 1$ ppmv) correspond to also very low N_{ice} of large sizes (Figs. 4h,i), indicating cirrus formed in high latitudes and reflecting calm conditions and low concentrations of INPs at high latitudes.

In summary, during CIRRUS-HL, a wide variety of atmospheric conditions and cirrus with different microphysical properties were sampled, ranging from very thick convective liquid origin to very thin in situ–origin cirrus and contrail cirrus. We found larger ice crystals associated with an order of magnitude lower ice crystal number concentrations in the Arctic than at midlatitudes (De La Torre Castro et al. 2023). This is potentially related to the combination of low INP concentrations and low updrafts at high latitudes and the higher amount of air traffic and convection at midlatitudes.

b. Aerosol and trace gas distribution in high and midlatitudes. Flight strategies and targeted altitudes during CIRRUS-HL focused not only on the cirrus altitudes but also on the full vertical distribution of aerosol and trace gases, scanning the atmosphere from the boundary layer to the stratosphere. Figure 5 shows altitude profiles of median aerosol and trace gas distributions, with 25th and 75th percentiles of the distribution in equidistant altitude bins. Aerosol number concentrations (Figs. 5a,b) were measured using a condensation particle counter (CPC) of the Aerosol Measurement System with CPCs/PSAP/SP2xr (AMETYST) instrument with a lower cutoff diameter of 12 nm. In Fig. 5a, we compare the midlatitude profile with measurements during the COVID-19 lockdown period during the BLUESKY mission (Voigt et al. 2022) and a 10-yr dataset of aerosol measurements in June and July for the region covered by CIRRUS-HL in pre-COVID-19 times from the Civil Aircraft for Remote Sensing and In Situ Measurements in Troposphere and Lower Stratosphere Based on the Instrumentation Container (CARIBIC) project (Zahn et al. 2024). As CIRRUS-HL took place during a period of increasing anthropogenic activity including air traffic, mean aerosol number concentrations in the free troposphere are mostly above the BLUESKY measurements but still reduced by 40%–80% compared to the CARIBIC dataset. Mean near-surface (<3 km) levels of aerosol particles (Figs. 5a,b) and of combustion-related trace gases such as carbon monoxide (CO)

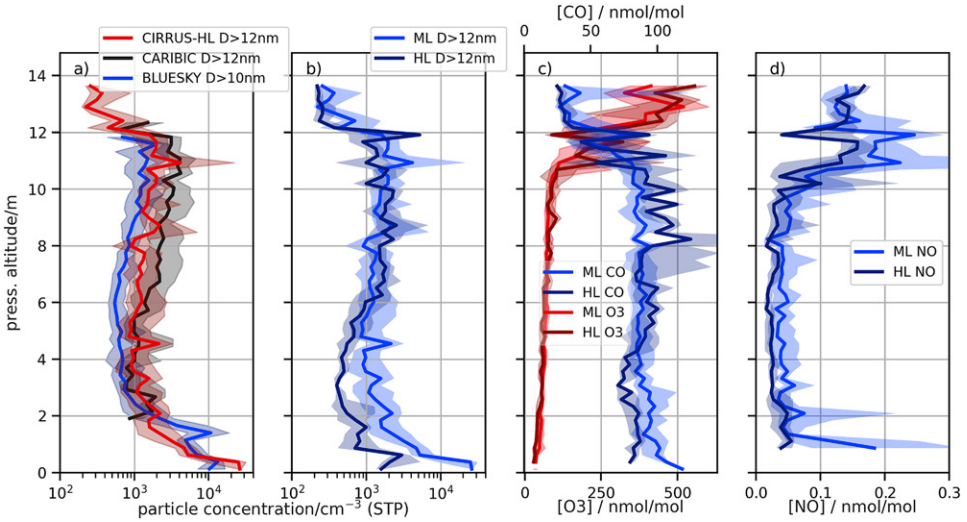

Fig. 5. Altitude profiles of aerosol and trace gases for high and midlatitudes. (a) Median midlatitude aerosol number concentration profiles from CIRRUS-HL (*D* > 12 nm), BLUESKY (*D* > 10 nm) (Voigt et al. 2022), and CARIBIC (*D* > 12 nm) (Zahn et al. 2024), where *D* is the lower cutoff diameter of the CPC measurement. (b) CIRRUS-HL high- and midlatitude aerosol profiles of total aerosol number concentrations at standard conditions (STP). (c) Median FAIRO O_3 (red) and Picarro CO (blue) mole fractions. (d) Median AENEAS NO mole fractions. In (b)–(d), light colors represent midlatitude measurements (<60°N), and darker colors represent high-latitude measurements (>60°N). In all panels, shaded areas indicate the range between the 25th and 75th percentiles, and solid lines refer to the median.

and NO (Figs. 5c,d) were enhanced in midlatitudes compared to high latitudes, related to the greater anthropogenic activity in midlatitudes. In the free troposphere (between 6 and 10 km), this trend is inverted, potentially due to cloud scavenging effects on black carbon and other aerosol particles (Zieger et al. 2023). Further, LAGRANTO backward-trajectory calculations indicate that long-range transport of biomass burning emissions from Siberia and North America led to elevated aerosol and CO levels during some events, exceeding 200 ppbv in the upper Arctic troposphere. One case reaching the stratosphere, measured on 7 July 2021, is shown in Fig. 8. In flight corridors, the aerosol concentrations are higher in the midlatitudes. The NO concentration profile (Fig. 5d) generally shows higher median values in midlatitudes throughout the troposphere and is particularly enhanced at cruise altitudes. Given its short lifetime, elevated NO concentrations indicate fresh emissions. Main sources of NO in the upper troposphere are transport from the polluted boundary layer and in situ production by lightning (Schumann and Huntrieser 2007) and air traffic (Jurkat et al. 2011). All sources are more pronounced at midlatitudes than at higher latitudes. At the altitude of cirrus formation, we find a significantly smaller difference in mean total aerosol number concentration from high to midlatitudes compared to the mean ice crystal number concentration (almost one order of magnitude). Future studies will concentrate on the distribution of INPs to assess the impact on cirrus cloud formation at high and midlatitudes.

c. Water vapor distribution in high and midlatitudes. Upper-tropospheric humidity is a key quantity for cirrus formation and life cycle (Diao et al. 2015) and governs the formation, persistence, and microphysical properties of contrails and their evolution into contrail cirrus (Schumann et al. 2015; Verma and Burkhardt 2022; Wang et al. 2025). We provide in Fig. 6a a distribution of the frequency of occurrence of relative humidity with respect to ice (RHi) at temperatures below 235 K from all humidity sensors aboard HALO during CIRRUS-HL. The distributions are given for measurements inside clouds from SHARC and clear-sky conditions from WALES, FISH, AIMS, and SHARC [for H_2O < 80 ppmv in light colors]. The instruments and derived RHi from temperature measurements aboard HALO (Giez et al. 2021) and ECMWF temperature fields agree well within their respective measurement and uncertainty range (Kaufmann et al. 2018), providing a clear picture of the humidity for ambient temperatures below 235 K. While each instrument has an uncertainty of less than 10% for the measurement of water vapor concentrations, the

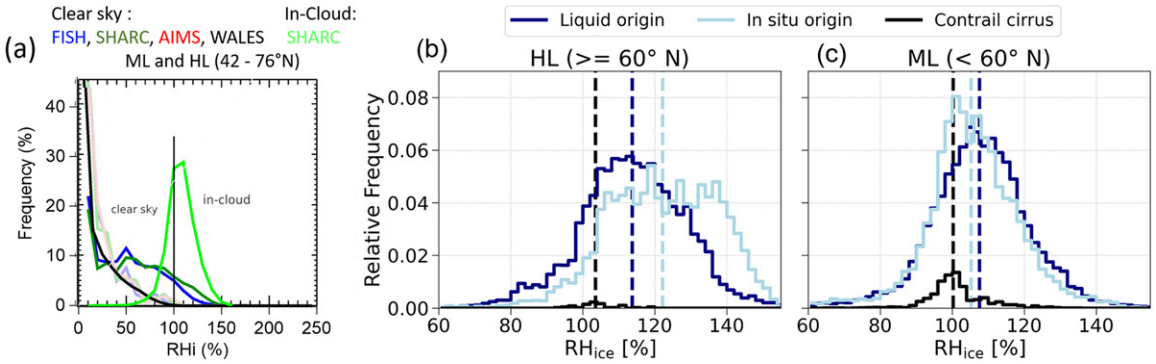

Fig. 6. Overview of RHi measurements during CIRRUS-HL. (a) Frequency distributions for mid- and high latitudes and temperatures $\lesssim$ 235K (based on more than 30 000 data points for each distribution): (i) clear-sky conditions from SHARC and FISH and selected for UT values (H_2O < 80 ppmv) for SHARC, FISH, AIMS, and WALES; (ii) in-cloud conditions from SHARC. (b),(c) In-cloud relative frequency distribution from SHARC, separated into three cloud types: in situ (light blue), liquid-origin (navy), and contrail (black) cirrus for (b) high- and (c) midlatitude cirrus. Medians of contrail cirrus, liquid-origin, and in situ–origin cirrus range from 100% (ML contrail cirrus) to 105% (ML in situ) and 122% (HL in situ) and are marked with dashed lines.

uncertainty of the derived RHi is on the order of 10%–12% due to the additional uncertainty of the temperature measurement (Kaufmann et al. 2018). The summer upper troposphere during CIRRUS-HL exhibits a high-occurrence frequency of supersaturated air, both inside the clouds and in clear-sky conditions. Inside the clouds, a median RHi of 107% is found, with 25th and 75th percentiles of 99% and 140%, respectively. From the FISH and SHARC measurements, it is found that 8% and 14% of the clear-sky data are supersaturated, respectively. We compare the SHARC RHi frequency distributions in liquid-origin and in situ–origin cirrus next to contrail cirrus for high and midlatitudes. Medians (indicated by dashed vertical lines) of RHi distributions in all naturally formed cirrus types are above saturation. The highest values of in-cloud supersaturation have been found in the high latitudes inside in situ–origin cirrus. These thin cirrus with low ice crystal numbers were mostly formed in the pristine Arctic regions with a reduced number of INPs, potentially related to the lower levels of pollution (Ovarlez et al. 2002; Jensen et al. 2001). During CIRRUS-HL, contrails and contrail cirrus are often detected in regions with high RHi inside or at the top of cirrus (see Fig. 9) (Jensen et al. 1998; Dekoutsidis et al. 2023). These observations are in contrast to previous measurements in spring (Voigt et al. 2017) where contrail cirrus were mainly observed in subsaturated conditions (Li et al. 2023). We explain the systematically supersaturated conditions (median values above 100%) observed in midlatitudes with two flights in convectively forced cirrus during summer, which due to higher updrafts may have altered the RHi spectrum to higher supersaturation (Petzold et al. 2017; D'Alessandro et al. 2017). During transfer from Oberpfaffenhofen to higher latitudes, we frequently flew at cloud tops, some of them convectively forced, where enhanced supersaturation is often observed (Diao et al. 2014a,b; Dekoutsidis et al. 2023). In high latitudes, the reduced number of INPs and the thin cirrus of low number concentrations (Krämer 2009; Patnaude et al. 2021) and surface area do not provide a large condensational sink to relax RHi to 100%. The median RHi in contrail cirrus is shown in black in Figs. 6b and 6c. Due to the typically high number concentration of ice crystals ($N_{ice} > 0.1$ cm^{-3}) with low EDs ($< 40\ \mu$m), the RHi median relaxes toward saturation, as previously observed in young contrails (Kaufmann et al. 2014). This observation indicates the relevance of contrail cirrus as an effective sink of ambient supersaturation, thereby suppressing new particle formation and particle growth (Schumann et al. 2015).

7. Selected results from the CIRRUS-HL mission

This section provides selected results from individual flights during CIRRUS-HL. The combination of measurements and models from these flights gives short insights into the flight strategies, the regions, and the multitude of applications and research topics that CIRRUS-HL targeted. We first focus on one case study on natural Arctic clouds and on aerosol and ice particle residual properties and radiation measurements. The last two selected results focus on contrail cirrus measurements and modeling.

a. Impact of a high-latitude cirrus on the radiation budget. To quantify the impact of cirrus on the Arctic radiative budget, ice crystal optical properties and spectral albedo were assessed during CIRRUS-HL. On 29 June 2021, a staircase flight pattern analyzed a high-level warm front cirrus north of Iceland, consisting of flight legs below, within, and above it. Figure 7a shows the predicted ice and liquid water contents across the HALO flight path from the ECMWF's 1200 UTC analysis. Flight leg 5, the system's center, recorded the highest LWP (Fig. 7b).

The impact of the clouds on the spectral albedo measured by SMART is indicated in Fig. 7d for each flight leg. Two dependencies are obvious. The albedo in the visible spectrum (e.g., around 500-nm wavelength) increases with increasing amounts of liquid and

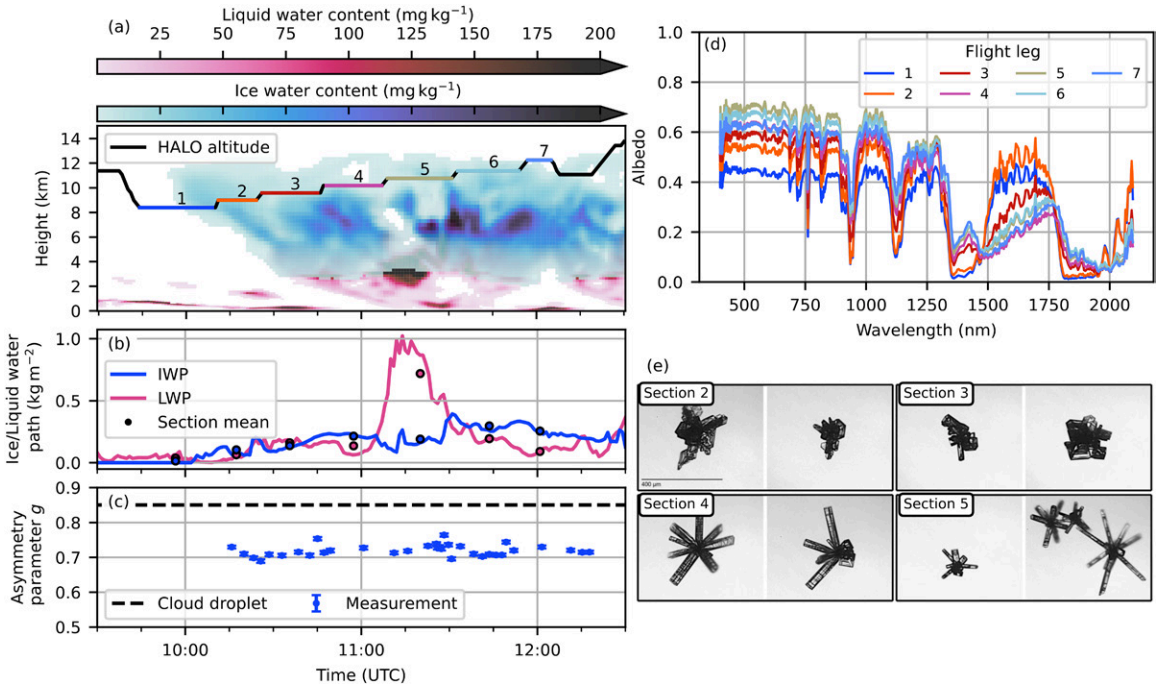

Fig. 7. Investigation of an Arctic cloud. (a) Staircase flight pattern from F05 on 29 Jun 2021 shown together with a cross section of IWC and LWC from the 1200 UTC analysis of the ECMWF's IFS. (b) Ice water path (IWP) and LWP along track with the section mean from the IFS's 1200 UTC analysis. (c) Mean asymmetry parameter *g* along the flight track. (d) Mean spectral albedo for the seven staircase sections. (e) Collage of ice crystal images from different sections.

ice water below HALO as calculated from the model. This spectral range also dominates the broadband albedo. The lowest albedo is found in flight leg 1, while the maximum albedo is observed in flight leg 5. Analyzing the spectral albedo in the near-infrared region between 1500 and 1750 nm, where absorption of the ice and liquid particles is apparent, allows for characterizing the impact of cloud thermodynamic phase (Ehrlich et al. 2008). Flight legs 1 and 2 show a high albedo in this spectral range, and thus, the albedo is still mostly influenced by the lower-level liquid cloud. Starting with flight leg 3, the impact of the ice cloud on the spectral albedo becomes apparent. Figure 7c shows the asymmetry parameter *g* retrieved from the Particle Habit Imaging and Polar Scattering (PHIPS) measurements using the methodology presented in Xu et al. (2022) and its standard deviation along the flight track. A total of 1716 crystals were sampled, and one retrieved *g* value corresponds to a population of 50 crystals (about 19-L volume). Measured *g* values ranged from 0.69 to 0.76, averaging 0.72, indicating the presence of complex crystals. This is in agreement with the high-resolution microscopic single-particle images (Fig. 7e). Despite the variety in crystal shapes across different flight legs—with flight leg 2 dominated by 72% side planes, flight leg 3 showing 54% irregular polycrystals, and higher altitudes featuring over 70% bullet rosettes—*g* showed minimal variation. This finding contradicts higher *g* values typically used in radiative transfer simulations, highlighting the potential underestimation of cirrus cloud reflectivity. Therefore, direct measurements of ice crystal single-scattering properties in combination with spectral albedo measurements can be used to assess the current representation by ice optical parameterizations in numerical models and eventually to develop new optical parameterizations.

b. Measurements of cirrus particle residuals, upper-tropospheric fine-mode aerosol particles, and their ice nucleation ability. Selected results from research flights F08 to F11 representing different atmospheric conditions are presented here: lower-stratospheric (LS) biomass burning (BB) aerosol (LS_BB_aerosol, F10/F11) identified through chemical

single-particle composition analysis, LS aerosol (LS_aerosol, F08/F09), upper-tropospheric (UT) aerosol (UT_aerosol, F10/F11), and UT cirrus particle residuals (UT_residuals, F10/F11). According to backward-trajectory analysis and satellite images, the LS_BB_aerosol likely originated from wildfires in British Columbia, Canada, where pyrocumulonimbus clouds reached the UTLS 7 days prior to our measurements.

As illustrated in Fig. 8a, the background concentrations of large particles (≥500 nm) were similarly low for UT_aerosol (green) as for LS_aerosol (gray), but the concentration of Aitken mode particles (≤100 nm) was much higher for UT_aerosol, which may be due to UT aerosol formation (e.g., Brock et al. 1995). As the LS_BB_aerosol (orange) exhibited no enhanced Aitken mode but markedly higher concentrations of accumulation mode particles (≥200 nm), we suggest that BB smoke had no major impact on the Aitken mode aerosol in the LS. Similar to the UT_aerosol concentration, the UT_residuals (blue) also show a maximum in the

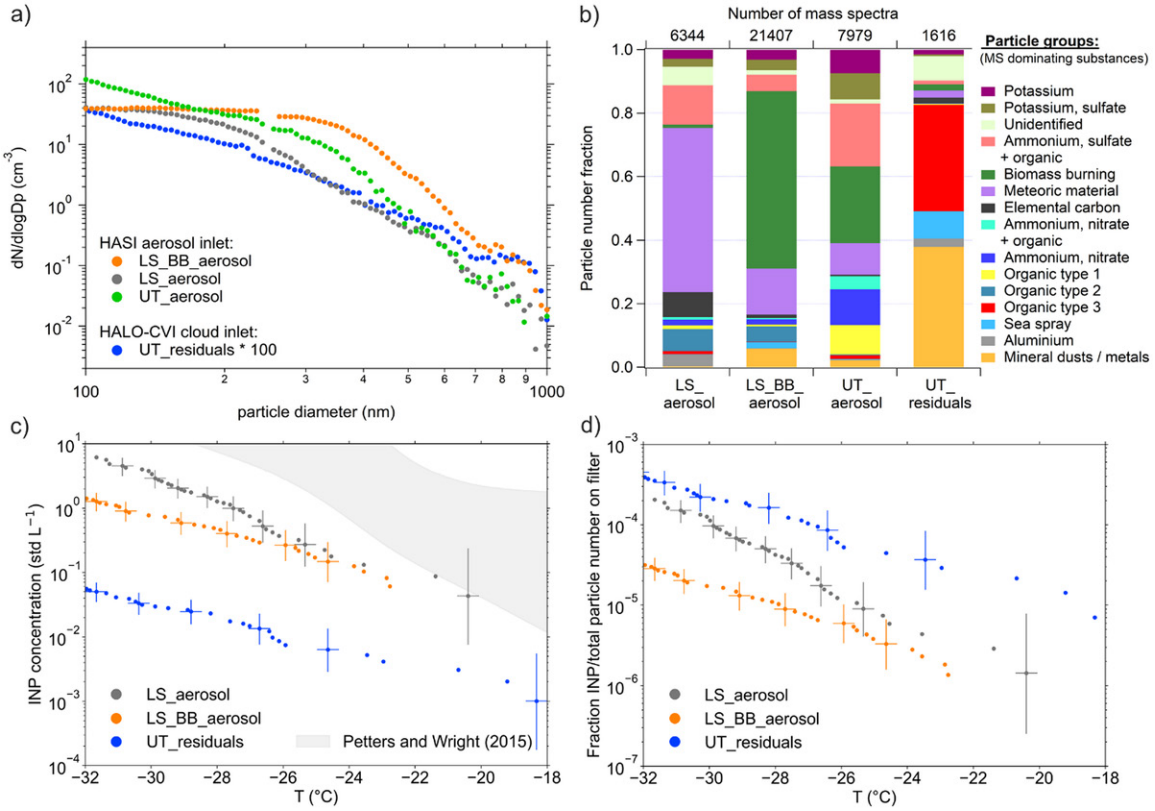

Fig. 8. Physical and chemical characteristics of aerosol particles and cirrus particle residuals under different atmospheric conditions, i.e., LS BB aerosol (LS_BB_aerosol, F10/F11, averaged O_3 concentration and altitude during measurement: 474 ppb and 13317 m), LS aerosol (LS_aerosol, F08/F09, 450 ppb and 13150 m), UT aerosol (UT_aerosol, F10/F11, 83 ppb and 10564 m), each sampled through the HASI inlet, and UT cirrus particle residuals (UT_residuals, F10/F11, 81 ppb and 10406 m) sampled through the HALO-CVI. Averaged ambient air temperature ranged between 223 and 227 K during the four periods. (a) Aerosol particle size distributions during the time periods described above measured with the FASD-UHSAS and cirrus particle residual size distribution measured with the CVI-UHSAS. The size distribution for the cirrus particle residuals is scaled by a factor of 100 for better comparison. (b) Composition of the aerosol particle and the cirrus particle residual population determined with the ALABAMA. Particles are sorted into groups according to those ion peaks that dominate the individual mass spectra. (c) INP concentrations per liter of sampled air from HERA filters as a function of freezing temperature. The gray area in the background shows typical tropospheric INP concentrations from midlatitudes (Petters and Wright 2015). Sampling volumes were calculated for standard conditions [T = 273.15 K; p = 1013.25 mb (1 mb = 1 hPa)] and in the case of the CVI filter normalized with the average enrichment factor of the sampling period. (d) Temperature-dependent INP fraction (INP number divided by total number of aerosol particles or cirrus residual particles sampled on HERA filters). Aerosol particle concentrations were taken from the FASD-UHSAS, and cirrus residual particle concentrations were taken from the CVI-UHSAS.

Aitken mode size range, in line with earlier size distribution measurements of cirrus particle residuals (Seifert et al. 2003). This feature is also commonly found for ice particle residuals in mixed-phase clouds (Mertes et al. 2007; Kupiszewski et al. 2016), which are formed by heterogeneous ice nucleation, suggesting that this mechanism was observed in the investigated cirrus clouds, too. Figure 8b shows the particle groups resulting from the mass spectrometric analysis. For LS_aerosol, the particle group "meteoric material" (e.g., Murphy et al. 1998; Schneider et al. 2021) was by far the most frequently observed. Furthermore, in comparison with the other sampling periods, a higher fraction of the particle group "elemental carbon" and, in comparison with UT_aerosol, a higher fraction of the particle group "organic type 2" were observed. For LS_BB_aerosol, mainly particles indicating BB were identified. For these samples, a higher fraction of mineral dust and sea salt particles compared to LS_aerosol was observed. These particles may have been lifted to the UTLS within the pyrocumulonimbus (e.g., Andreae et al. 2004). The UT_aerosol is used in direct comparison with UT_residuals since both measurements took place during F10/F11 under similar conditions (altitude, temperature, ozone, time of day, and location). The composition of the UT_residuals is dominated by "organic type 3," sea salt, and mineral dust, which together account for about 80% of the particles. In contrast, these three particle groups account for less than 4% of the UT_aerosol, indicating that heterogeneous ice nucleation was important in the formation of the cirrus cloud particles sampled during F10/F11. Figure 8c shows the temperature-dependent INP concentrations derived from HERA for filters sampled during LS_BB_aerosol, LS_aerosol, and UT_residuals under similar conditions. The LS_aerosol filter can be regarded as representative of the background INP concentrations prevailing in the LS. Looking at Fig. 8c, it becomes obvious that LS background INP concentrations (STP) were significantly lower than typical midlatitude tropospheric INP concentrations, as derived from precipitation samples (gray area; Petters and Wright 2015). Astonishingly, INP concentrations in the LS_BB_aerosol were found to be lower than those representative of the LS background; i.e., seemingly, LS_BB_aerosol particles are not significantly contributing to the LS INP population. To allow for direct comparison, the number of INPs per filter was normalized with the total number of aerosol particles or cirrus particle residuals per filter retrieved from the FASD- and CVI-UHSAS, respectively (Fig. 8d). The UT_residuals featured a higher relative number of INPs compared to LS_aerosol and LS_BB_aerosol. Nonetheless, at −30 °C, the fraction of immersion freezing INPs versus the total number of residuals was only slightly above 0.02%, suggesting that immersion freezing above −30°C only played a minor role in forming ice crystals in these cirrus clouds. Either the ice crystals are formed by other, potentially more numerous immersion INP below −30°C or via other pathways such as homogeneous freezing and secondary ice production. The low fraction of INP in the LS_BB_aerosol suggests an insignificant contribution of BB aerosol particles to the INP population.

c. Remote sensing of contrails and contrail cirrus above Germany. Contrail and contrail cirrus predicted by the CoCiP model were targeted in CIRRUS-HL flights above Europe. One case of contrails and related fall streaks was observed by remote sensing instrumentation on 25 June 2021. The coincident measurements of backscatter ratio and particle depolarization at 532.1 nm from the HSRL WALES shown in Figs. 9d and 9e show vertical cross sections of two mixing cloud systems with different origins represented by a high and low depolarization ratio (Fig. 9e) (Urbanek et al. 2018). The first section of the cloud (before 1422 UTC) was influenced by a southerly flow, while the second part had a more pristine character with air masses coming from northern latitudes. Above upper-level cloud tops, water reached saturation with respect to ice also measured by WALES (Fig. 9f between 1416 and 1424 UTC) (Groß et al. 2014), which allowed the formation of persistent contrails. The high backscatter ratios (Fig. 9e) at the top of the cloud indicate contrails and related fall streaks (Sassen 1997;

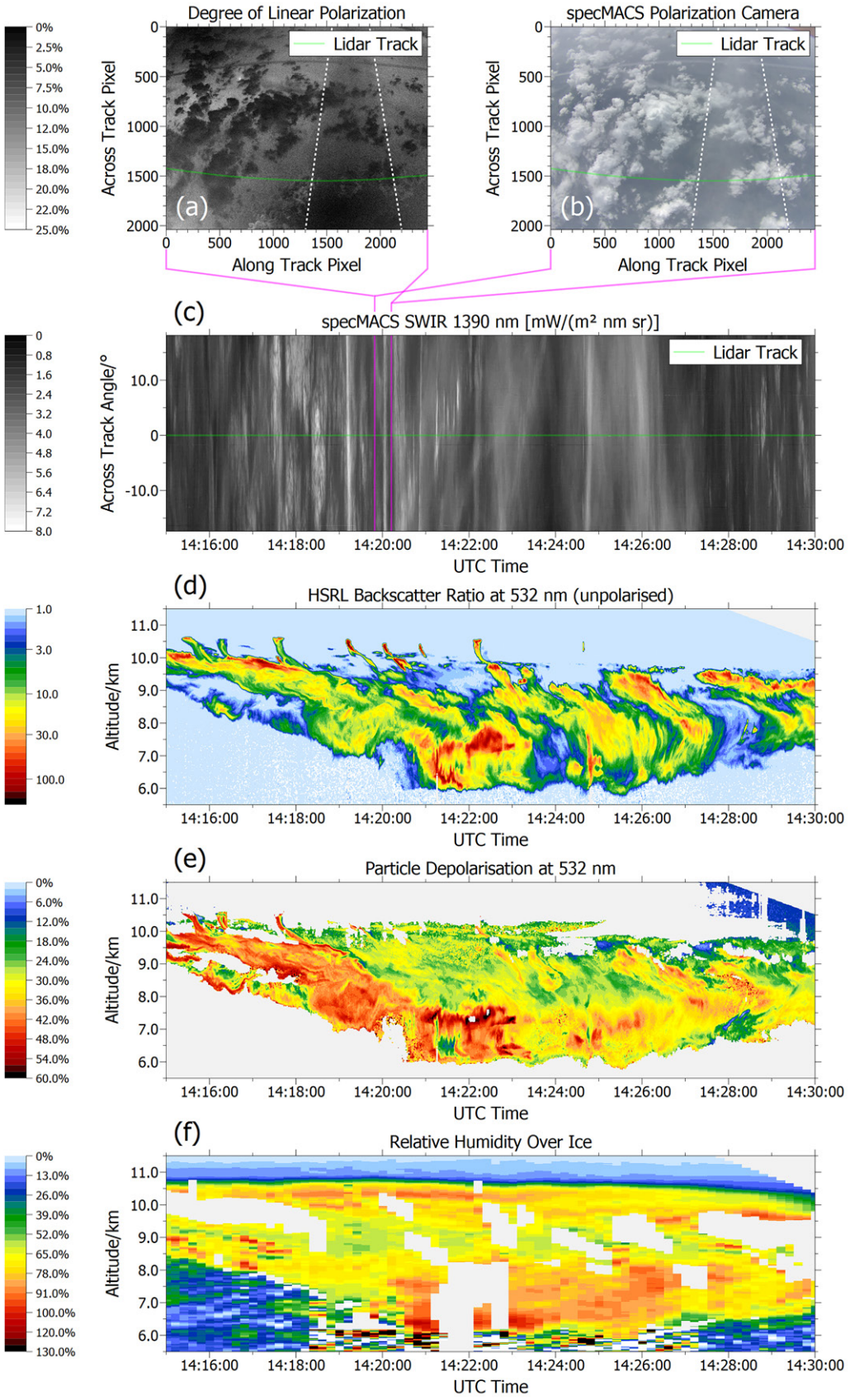

Fig. 9. 3D observations of contrails formed at the upper-level cloud tops. (a) Degree of linear polarization and (b) RGB image from the specMACS polarization camera at 1420 UTC. Dashed lines indicate the position of a young contrail. (c) 2D radiance measurement from specMACS at 1390 nm. (d) WALES backscatter ratio at 532 nm of young contrails and cirrus during one flight on 25 Jun 2021 observed above Germany. (e) Simultaneous measurement of particle depolarization at 532 nm from WALES. (f) Relative humidity over ice from WALES and ECMWF temperature.

Jensen et al. 1998; Unterstrasser et al. 2017) with ages of several minutes extending vertically several hundred meters below the flight altitude into the cirrus deck. In the upper, dense part of the contrail, no particle depolarization could be measured due to a saturated signal. Previous measurements have shown that contrail-to-cirrus evolution causes a change in the scattering phase functions and the asymmetry parameter g (Gayet et al. 2012; Chauvigné et al. 2018). The sedimenting contrail ice crystals locally modify the particle depolarization of the cloud below. This change in depolarization from the contrails has been observed simultaneously by the downward-looking hyperspectral and polarized imager specMACS (Ewald et al. 2016; Weber et al. 2024). Figures 9a and 9b show the degree of linear polarization and the corresponding RGB image measured by the polarization cameras. The images highlight an optically thin-line-shaped contrail oriented in the across-track direction, which corresponds to the contrail measured by WALES at 1420 UTC. An optically thin cirrus and a layer of small cumulus clouds are visible below. The contrails have a smaller degree of linear polarization and appear darker in Fig. 9a. Furthermore, the cloud glint, which is formed by specular reflection on oriented ice crystals, is visible as a narrow bright spot in the upper-left corner and indicates the presence of oriented ice crystals in the cirrus. Moreover, the cloudbow, which forms by scattering on liquid cloud droplets in the lower cumulus layer, appears as a bow of enhanced polarization in the lower right and has been evaluated to determine the droplet size distribution (Pörtge et al. 2023). The various contrails measured by WALES are also visible as white thin lines along the across-track angle perspective in the observation of the hyperspectral camera of specMACS at 1390 nm in Fig. 9c. These stripes coincide with the higher backscatter ratio of WALES. We chose a wavelength of 1390 nm with strong water vapor absorption so that, in contrast to the RGB image (visible wavelength range), only high clouds above the absorbing layers are visible.

The coincident measurements give 3D information of young contrails above a thin cirrus deck, providing evidence on the change in the polarization of the incident light due to the contrails and in contrast to the natural cirrus below.

d. Cloud-radiative forcing as observed from satellite observations with CoCiP model studies. Satellite observations can give a general overview of contrail cirrus and natural cirrus conditions in a large spatial scale. Due to smaller crystal sizes, young contrails tend to show higher brightness temperature differences [BTDs (10.8 – 12.0) and channel 10.8 minus 12.0 μm] compared to natural cirrus (e.g., Mannstein et al. 1999). We conducted an analysis of optical properties and radiative impact of contrail cirrus based on Meteosat Second Generation (MSG) satellite observations and compared the results with CoCiP simulations at 1000 UTC 21 July 2021. CoCiP simulations adopted a humidity correction methodology (Teoh et al. 2022a) to improve the input RHi derived from ECMWF data. This correction accounts for the dry bias observed in the upper troposphere (Teoh et al. 2022b; Gierens et al. 2020; Wang et al. 2025) and its consequential influence on the persistence and climate impact of contrail cirrus. In Fig. 10a, an outbreak of contrail cirrus, represented by white areas, is situated over low-level liquid clouds, indicated by yellow regions, spanning the North Atlantic Ocean and the Iberian Peninsula. The flight path of HALO marked with a yellow line reflects the occurrence of scattered ice clouds with diameters larger than 3 μm measured with the CCP (purple shading). The linear-shaped contrails are clearly depicted as white lines in the BTD image in Fig. 10b. Satellite observations in Fig. 10c processed with the Cirrus Properties from SEVIRI (CiPS; Strandgren et al. 2017) algorithm reveal a contrail optical thickness of approximately 0.35, similar to the results in Wang et al. (2023), which aligns closely with the corresponding CoCiP simulations displayed in Fig. 10d. However, CiPS is not able to detect all contrails that can be observed by eye in the RGB composite in Fig. 10b. Examining the radiative effects, contrails in Fig. 10e exhibit a positive net cloud RF of

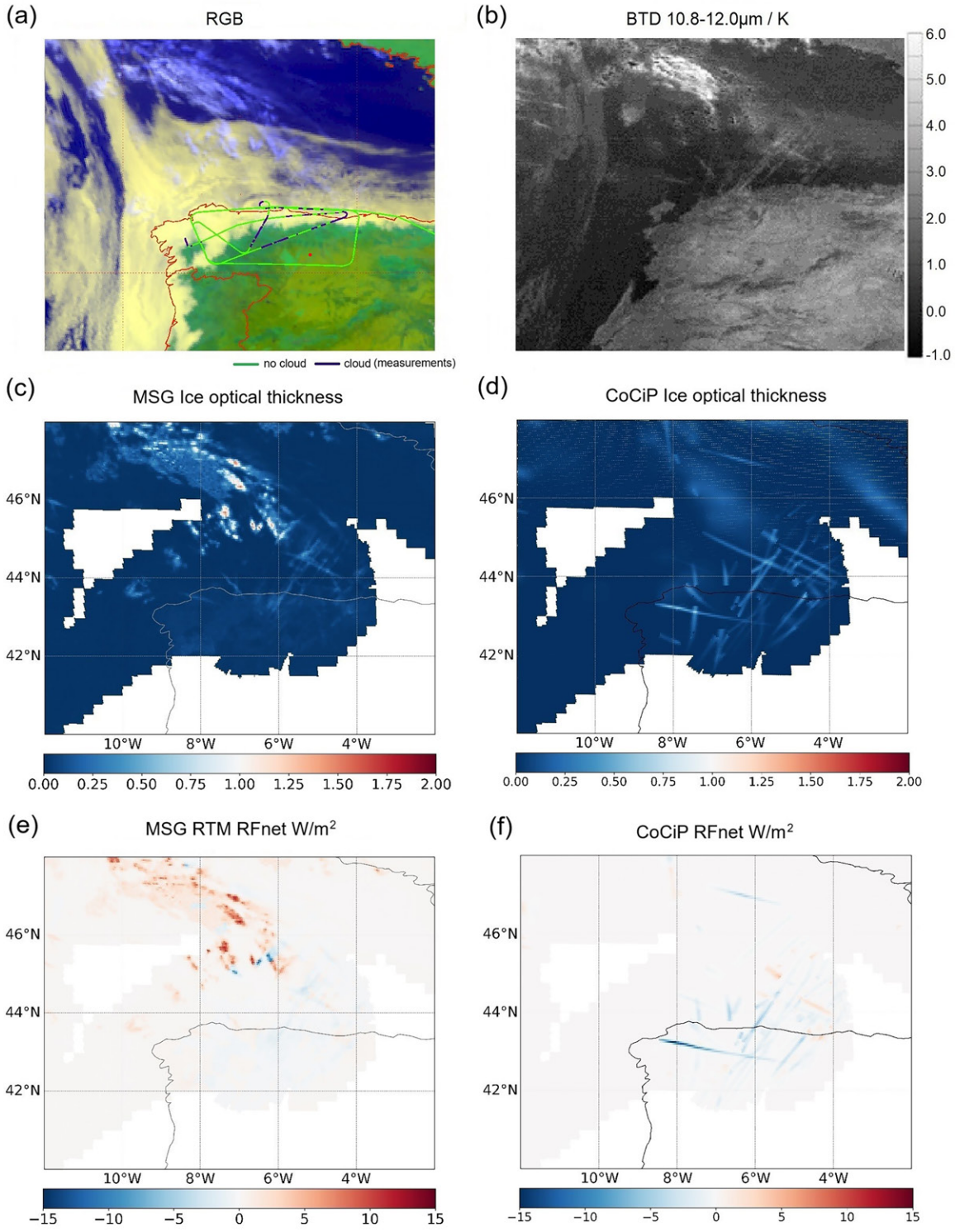

Fig. 10. Microphysical properties and radiative effects of a contrail cirrus outbreak over the North Atlantic Ocean and northern Portugal and Spain on 21 Jul 2021. (a) RGB with a yellow line representing the HALO flight path and purple colors representing the contrail cirrus cloud flag from CCP for ice crystals larger than 3 μm. (b) BTD. (c) Contrail cirrus optical thickness from MSG observations. (e) Net RF through satellite-observation-based radiative transfer modeling. (d),(f) Equivalent parameters of (c) and (e) but simulated by the CoCiP model. Values in (c)–(f) are masked with CoCiP-simulated cirrus grid boxes.

approximately 5–10 W m^{-2} over the ocean surface, in contrast to a negative net RF of about −5 W m^{-2} over northern Portugal and Spain, derived from satellite-observation-based radiative transfer modeling as in Wang et al. (2023). Contrails forming above low-level clouds with a high albedo in this case over ocean are more likely to be warming because the incoming

solar radiation would have been reflected by the low-level clouds regardless of the presence of contrails, thereby reducing the contrail shortwave (SW) RF (Teoh et al. 2022a). CoCiP simulations, as illustrated in Fig. 10f, also present the warming–cooling contrast in the radiative effects of contrail cirrus, with the net RF over the continent tending toward a more cooling effect. The reason for this can be attributed to the somewhat greater optical thickness and increased reflection observed in the CoCiP simulation, as shown in Fig. 10d. Future work will connect the airborne in situ and remote sensing data collected during flight to the satellite retrieval and model result presented here.

8. Summary and outlook

The HALO mission CIRRUS-HL provides a new dataset that includes a large spectrum of cloud, aerosol, trace gas, and radiation measurements in the midlatitude dense air traffic regions and in pristine Arctic regions in June and July 2021. Differences between high-latitude and midlatitude cirrus, aerosol, and trace gas distributions could be observed with influences from aviation, convectively formed cirrus, cirrus formed from the liquid phase (liquid-origin cirrus), and the vapor phase (in situ cirrus). Differences in the occurrence of supersaturation inside cirrus and the abundance of total aerosol number showed contrasting patterns from the Arctic to the midlatitudes. We examined cases of Arctic cirrus and contrail cirrus formed at the cloud tops of natural cirrus and contrail cirrus above low-level clouds to show the cloud-radiative effect and their impact on depolarization.

As the present paper provides an overview of the wide variety of cirrus measurements performed during CIRRUS-HL in different latitude ranges, the dataset invites a more detailed analysis of the different targets. Planned studies will provide an overview on microphysical properties of contrail cirrus categorized by age and thermodynamic state as a basis for model intercomparisons to improve our understanding on the interaction and modification of contrail cirrus with clouds and to reduce uncertainties on contrail cirrus radiative forcing estimates and on contrail prediction. Aviation as a source for in situ aerosol containing a high fraction of organic type 3 will be investigated based on the analysis of the composition of upper-tropospheric aerosol residuals. The influence of INP type and number on the formation of cirrus clouds measured during CIRRUS-HL will be the focus of another study to contrast the influence of anthropogenic (e.g., air traffic) and natural sources in mid- and high latitudes. The impact of the latitude dependence of cirrus on the linear depolarization ratio observed by the space-borne lidar CALIOP aboard *CALIPSO* will give further insight into the differences in the formation pathways of these cirrus based on a multiannual dataset. The sampling of two convective anvils during CIRRUS-HL offers the basis to investigate the impact on the local perturbation of LS water vapor through the injection of ice crystals in overshooting tops of convective systems. To study the indirect aviation effect on high and low clouds, the follow-up mission AERO–CLOUD will concentrate on aerosol–cloud effects from aircraft emissions such as the impact of sulfate particles on low-level clouds and the impact of soot emissions on cirrus properties and ISSR characterization. The data and results of CIRRUS-HL represent a valuable contribution to the international meteorological and aviation community through validation of weather forecasts, contrail prediction tools, and climate models.

Acknowledgments. We thank the DLR flight department for great support during the campaign and the pilots for excellent cooperation and flight guidance into cirrus and contrail cirrus. We thank Matthew A. Petroff for providing freely available scientific color maps, enhancing the visual quality of this work (@Petroff2021). Parts of the results in this work make use of the color maps in the CMasher package (@Vandervelden2020). J. S. and H. C. C. thank Katharina Kaiser (MPIC) for campaign support. H. C. C., E. D. C., L. T., J. M., T. J., and C. V. acknowledge funding by the

DFG through the SPP 1294 (HALO) under Grants SCHN 1138/8-1, VO1504/6-1, VO1504/7-1, and VO1504/9-1; TRR 301, project ID 428312742 and ID 522359172. R. A. acknowledges funding from the Swiss National Science Foundation (project 185049) and flight planning support by Hanin Binder, Maxi Boettcher, and Katharina Heitmann. C. B., J. H., and M. R. acknowledge funding from the DLR space research program (project MABAK) regarding the analysis of model data for flight planning.

Data availability statement. Processed data from the CIRRUS-HL campaign will become publicly available on the HALO database (https://doi.org/10.17616/R39Q0T) at https://halo-db.pa.op.dlr.de/mission/125 in June 2026. Earlier access to the data is available by contacting the first author.

References

Afchine, A., and Coauthors, 2018: Ice particle sampling from aircraft—Influence of the probing position on the ice water content. *Atmos. Meas. Tech.*, **11**, 4015–4031, https://doi.org/10.5194/amt-11-4015-2018.

Andreae, M. O., D. Rosenfeld, P. Artaxo, A. A. Costa, G. P. Frank, K. M. Longo, and M. A. F. Silva-Dias, 2004: Smoking rain clouds over the Amazon. *Science*, **303**, 1337–1342, https://doi.org/10.1126/science.1092779.

——, and Coauthors, 2018: Aerosol characteristics and particle production in the upper troposphere over the Amazon Basin. *Atmos. Chem. Phys.*, **18**, 921–961, https://doi.org/10.5194/acp-18-921-2018.

Bauer, R., J.-U. Grooß, J. Ungermann, May. Bär, M. Geldenhuys, and L. Hoffmann, 2022: The Mission Support System (MSS v7.0.4) and its use in planning for the SouthTRAC aircraft campaign. *Geosci. Model Dev.*, **15**, 8983–8997, https://doi.org/10.5194/gmd-15-8983-2022.

Baumgartner, M., C. Rolf, J.-U. Grooß, J. Schneider, T. Schorr, O. Möhler, P. Spichtinger, and M. Krämer, 2022: New investigations on homogeneous ice nucleation: The effects of water activity and water saturation formulations. *Atmos. Chem. Phys.*, **22**, 65–91, https://doi.org/10.5194/acp-22-65-2022.

Beer, C. G., and Coauthors, 2020: Modelling mineral dust emissions and atmospheric dispersion with MADE3 in EMAC v2.54. *Geosci. Model Dev.*, **13**, 4287–4303, https://doi.org/10.5194/gmd-13-4287-2020.

Bier, A., and U. Burkhardt, 2022: Impact of parametrizing microphysical processes in the jet and vortex phase on contrail cirrus properties and radiative forcing. *J. Geophys. Res. Atmos.*, **127**, e2022JD036677, https://doi.org/10.1029/2022JD036677.

——, S. Unterstrasser, J. Zink, D. Hillenbrand, T. Jurkat-Witschas, and A. Lottermoser, 2024: Contrail formation on ambient aerosol particles for aircraft with hydrogen combustion: A box model trajectory study. *Atmos. Chem. Phys.*, **24**, 2319–2344, https://doi.org/10.5194/acp-24-2319-2024.

Bock, L., and A. Lauer, 2024: Cloud properties and their projected changes in CMIP models with low to high climate sensitivity. *Atmos. Chem. Phys.*, **24**, 1587–1605, https://doi.org/10.5194/acp-24-1587-2024.

Brands, M., and Coauthors, 2011: Characterization of a newly developed Aircraft-based Laser ABlation Aerosol Mass spectrometer (ALABAMA) and first field deployment in urban pollution plumes over Paris during MEGAPOLI 2009. *Aerosol Sci. Technol.*, **45**, 46–64, https://doi.org/10.1080/02786826.2010.517813.

Brock, C. A., P. Hamill, J. C. Wilson, H. H. Jonsson, and K. R. Chan, 1995: Particle formation in the upper tropical troposphere: A source of nuclei for the stratospheric aerosol. *Science*, **270**, 1650–1653, https://doi.org/10.1126/science.270.5242.1650.

Burkhardt, U., and B. Kärcher, 2011: Global radiative forcing from contrail cirrus. *Nat. Climate Change*, **1**, 54–58, https://doi.org/10.1038/nclimate1068.

Cai, Y., D. C. Montague, W. Mooiweer-Bryan, and T. Deshler, 2008: Performance characteristics of the ultra high sensitivity aerosol spectrometer for particles between 55 and 800 nm: Laboratory and field studies. *J. Aerosol Sci.*, **39**, 759–769, https://doi.org/10.1016/j.jaerosci.2008.04.007.

Chauvigné, A., and Coauthors, 2018: Statistical analysis of contrail to cirrus evolution during the CONtrail and Cirrus Experiment (CONCERT). *Atmos. Chem. Phys.*, **18**, 9803–9822, https://doi.org/10.5194/acp-18-9803-2018.

Chen, T., W. B. Rossow, and Y.-C. Zhang, 2000: Radiative effects of cloud-type variations. *J. Climate*, **13**, 264–286, https://doi.org/10.1175/1520-0442(2000)013<0264:REOCTV>2.0.CO;2.

Clemen, H.-C., and Coauthors, 2020: Optimizing the detection, ablation, and ion extraction efficiency of a single-particle laser ablation mass spectrometer for application in environments with low aerosol particle concentrations. *Atmos. Meas. Tech.*, **13**, 5923–5953, https://doi.org/10.5194/amt-13-5923-2020.

D'Alessandro, J. J., and Coauthors, 2017: Dynamical conditions of ice supersaturation and ice nucleation in convective systems: A comparative analysis between in situ aircraft observations and WRF simulations. *J. Geophys. Res. Atmos.*, **122**, 2844–2866, https://doi.org/10.1002/2016JD025994.

Dekoutsidis, G., S. Groß, M. Wirth, M. Krämer, and C. Rolf, 2023: Characteristics of supersaturation in midlatitude cirrus clouds and their adjacent cloud-free air. *Atmos. Chem. Phys.*, **23**, 3103–3117, https://doi.org/10.5194/acp-23-3103-2023.

De La Torre Castro, E., and Coauthors, 2023: Differences in microphysical properties of cirrus at high and mid-latitudes. *Atmos. Chem. Phys.*, **23**, 13167–13189, https://doi.org/10.5194/acp-23-13167-2023.

Diao, M., M. A. Zondlo, A. J. Heymsfield, L. M. Avallone, M. E. Paige, S. P. Beaton, T. Campos, and D. C. Rogers, 2014a: Cloud-scale ice-supersaturated regions spatially correlate with high water vapor heterogeneities. *Atmos. Chem. Phys.*, **14**, 2639–2656, https://doi.org/10.5194/acp-14-2639-2014.

——, ——, ——, and S. P. Beaton, 2014b: Hemispheric comparison of cirrus cloud evolution using in situ measurements in HIAPER Pole-to-Pole Observations. *Geophys. Res. Lett.*, **41**, 4090–4099, https://doi.org/10.1002/2014GL059873.

——, J. B. Jensen, L. L. Pan, C. R. Homeyer, S. Honomichl, J. F. Bresch, and A. Bansemer, 2015: Distributions of ice supersaturation and ice crystals from airborne observations in relation to upper tropospheric dynamical boundaries. *J. Geophys. Res. Atmos.*, **120**, 5101–5121, https://doi.org/10.1002/2015JD023139.

Ehrlich, A., E. Bierwirth, M. Wendisch, J.-F. Gayet, G. Mioche, A. Lampert, and J. Heintzenberg, 2008: Cloud phase identification of Arctic boundary-layer clouds from airborne spectral reflection measurements: Test of three approaches. *Atmos. Chem. Phys.*, **8**, 7493–7505, https://doi.org/10.5194/acp-8-7493-2008.

——, and Coauthors, 2023: A new airborne broadband radiometer system and an efficient method to correct dynamic thermal offsets. *Atmos. Meas. Tech.*, **16**, 1563–1581, https://doi.org/10.5194/amt-16-1563-2023.

Esselborn, M., M. Wirth, A. Fix, M. Tesche, and G. Ehret, 2008: Airborne high spectral resolution lidar for measuring aerosol extinction and backscatter coefficients. *Appl. Opt.*, **47**, 346–358, https://doi.org/10.1364/ao.47.000346.

Ewald, F., T. Kölling, A. Baumgartner, T. Zinner, and B. Mayer, 2016: Design and characterization of specMACS, a multipurpose hyperspectral cloud and sky imager. *Atmos. Meas. Tech.*, **9**, 2015–2042, https://doi.org/10.5194/amt-9-2015-2016.

Gasparini, B., A. Meyer, D. Neubauer, S. Münch, and U. Lohmann, 2018: Cirrus cloud properties as seen by the *CALIPSO* satellite and ECHAM-HAM global climate model. *J. Climate*, **31**, 1983–2003, https://doi.org/10.1175/JCLI-D-16-0608.1.

Gayet, J.-F., and Coauthors, 2012: The evolution of microphysical and optical properties of an A380 contrail in the vortex phase. *Atmos. Chem. Phys.*, **12**, 6629–6643, https://doi.org/10.5194/acp-12-6629-2012.

Gierens, K., 2021: Theory of contrail formation for fuel cells. *Aerospace*, **8**, 164, https://doi.org/10.3390/aerospace8060164.

——, S. Matthes, and S. Rohs, 2020: How well can persistent contrails be predicted? *Aerospace*, **7**, 169, https://doi.org/10.3390/aerospace7120169.

Giez, A., C. Mallaun, V. Nenakhov, and M. Zöger, 2021: Calibration of a nose boom mounted airflow sensor on an atmospheric research aircraft by inflight maneuvers. Tech. Rep. DLR-Forschungsbericht DLR-FB-2021-17, 179 pp., https://elib.dlr.de/145969/.

Grawe, S., C. Jentzsch, J. Schaefer, H. Wex, S. Mertes, and F. Stratmann, 2023: Next-generation ice-nucleating particle sampling on board aircraft: Characterization of the High-volume flow aERosol particle filter sAmpler (HERA). *Atmos. Meas. Tech.*, **16**, 4551–4570, https://doi.org/10.5194/amt-16-4551-2023.

Groß, S., M. Wirth, A. Schäfler, A. Fix, S. Kaufmann, and C. Voigt, 2014: Potential of airborne lidar measurements for cirrus cloud studies. *Atmos. Meas. Tech.*, **7**, 2745–2755, https://doi.org/10.5194/amt-7-2745-2014.

——, T. Jurkat-Witschas, Q. Li, M. Wirth, B. Urbanek, M. Krämer, R. Weigel, and C. Voigt, 2023: Investigating an indirect aviation effect on mid-latitude cirrus clouds—Linking lidar-derived optical properties to in situ measurements. *Atmos. Chem. Phys.*, **23**, 8369–8381, https://doi.org/10.5194/acp-23-8369-2023.

Heckl, M., A. Fix, M. Jirousek, F. Schreier, J. Xu, and M. Rapp, 2021: Measurement characteristics of an airborne Microwave Temperature Profiler (MTP). *Atmos. Meas. Tech.*, **14**, 1689–1713, https://doi.org/10.5194/amt-14-1689-2021.

Heymsfield, A. J., and Coauthors, 2017: Cirrus clouds. *Ice Formation and Evolution in Clouds and Precipitation: Measurement and Modeling Challenges*, *Meteor. Monogr.*, No. 58, Amer. Meteor. Soc., https://doi.org/10.1175/AMSMONOGRAPHS-D-16-0010.1.

Hong, Y., and G. Liu, 2015: The characteristics of ice cloud properties derived from CloudSat and CALIPSO measurements. *J. Climate*, **28**, 3880–3901, https://doi.org/10.1175/JCLI-D-14-00666.1.

Järvinen, E., H. Wernli, and M. Schnaiter, 2018: Investigations of mesoscopic complexity of small ice crystals in midlatitude cirrus. *Geophys. Res. Lett.*, **45**, 11 465–11 472, https://doi.org/10.1029/2018GL079079.

Jensen, E. J., and Coauthors, 1998: Environmental conditions required for contrail formation and persistence. *J. Geophys. Res.*, **103**, 3929–3936, https://doi.org/10.1029/97JD02808.

——, and Coauthors, 2001: Prevalence of ice-supersaturated regions in the upper troposphere: Implications for optically thin ice cloud formation. *J. Geophys. Res.*, **106**, 17 253–17 266, https://doi.org/10.1029/2000JD900526.

Jöckel, P., and Coauthors, 2010: Development cycle 2 of the Modular Earth Submodel System (MESSy2). *Geosci. Model Dev.*, **3**, 717–752, https://doi.org/10.5194/gmd-3-717-2010.

Jurkat, T., and Coauthors, 2011: Measurements of HONO, NO, NOy and SO_2 in aircraft exhaust plumes at cruise. *Geophys. Res. Lett.*, **38**, L10807, https://doi.org/10.1029/2011GL046884.

——, S. Kaufmann, C. Voigt, D. Schäuble, P. Jeßberger, and H. Ziereis, 2016: The airborne mass spectrometer AIMS—Part 2: Measurements of trace gases with stratospheric or tropospheric origin in the UTLS. *Atmos. Meas. Tech.*, **9**, 1907–1923, https://doi.org/10.5194/amt-9-1907-2016.

Kaiser, J. C., J. Hendricks, M. Righi, N. Riemer, R. A. Zaveri, S. Metzger, and V. Aquila, 2014: The MESSy aerosol submodel MADE3 (v2.0b): Description and a box model test. *Geosci. Model Dev.*, **7**, 1137–1157, https://doi.org/10.5194/gmd-7-1137-2014.

——, and Coauthors, 2019: Global aerosol modeling with MADE3 (v3.0) in EMAC (based on v2.53): Model description and evaluation. *Geosci. Model Dev.*, **12**, 541–579, https://doi.org/10.5194/gmd-12-541-2019.

Kalinka, F., M. Butter, T. Jurkat, E. De La Torre Castro, and C. Voigt, 2023: A simple prototype to forecast high ice water content using TAT anomalies as training data. SAE Tech. Paper 2023-01-1495, https://doi.org/10.4271/2023-01-1495.

Kärcher, B., and U. Lohmann, 2002: A parameterization of cirrus cloud formation: Homogeneous freezing of supercooled aerosols. *J. Geophys. Res.*, **107**, 4010, https://doi.org/10.1029/2001JD000470.

——, and ——, 2003: A parameterization of cirrus cloud formation: Heterogeneous freezing. *J. Geophys. Res.*, **108**, 4402, https://doi.org/10.1029/2002JD003220.

Kaufmann, S., C. Voigt, P. Jeßberger, T. Jurkat, H. Schlager, A. Schwarzenboeck, M. Klingebiel, and T. Thornberry, 2014: In situ measurements of ice saturation in young contrails. *Geophys. Res. Lett.*, **41**, 702–709, https://doi.org/10.1002/2013GL058276.

——, and Coauthors, 2016: The airborne mass spectrometer AIMS—Part 1: AIMS-H_2O for UTLS water vapor measurements. *Atmos. Meas. Tech.*, **9**, 939–953, https://doi.org/10.5194/amt-9-939-2016.

——, and Coauthors, 2018: Intercomparison of midlatitude tropospheric and lower-stratospheric water vapor measurements and comparison to ECMWF humidity data. *Atmos. Chem. Phys.*, **18**, 16 729–16 745, https://doi.org/10.5194/acp-18-16729-2018.

Kay, J. E., T. L'Ecuyer, H. Chepfer, N. Loeb, A. Morrison, and G. Cesana, 2016: Recent advances in Arctic cloud and climate research. *Curr. Climate Change Rep.*, **2**, 159–169, https://doi.org/10.1007/s40641-016-0051-9.

Klausner, T., and Coauthors, 2020: Urban greenhouse gas emissions from the Berlin area: A case study using airborne CO_2 and CH_4 in situ observations in summer 2018. *Elementa*, **8**, 15, https://doi.org/10.1525/elementa.411.

Krämer, M., and Coauthors, 2009: Ice supersaturations and cirrus cloud crystal numbers. *Atmos. Chem. Phys.*, **9**, 3505–3522, https://doi.org/10.5194/acp-9-3505-2009.

——, and Coauthors, 2016: A microphysics guide to cirrus clouds—Part 1: Cirrus types. *Atmos. Chem. Phys.*, **16**, 3463–3483, https://doi.org/10.5194/acp-16-3463-2016.

——, and Coauthors, 2020: A microphysics guide to cirrus—Part 2: Climatologies of clouds and humidity from observations. *Atmos. Chem. Phys.*, **20**, 12 569–12 608, https://doi.org/10.5194/acp-20-12569-2020.

Krüger, K., A. Schäfler, M. Wirth, M. Weissmann, and G. C. Craig, 2022: Vertical structure of the lower-stratospheric moist bias in the ERA5 reanalysis and its connection to mixing processes. *Atmos. Chem. Phys.*, **22**, 15 559–15 577, https://doi.org/10.5194/acp-22-15559-2022.

Kuebbeler, M., U. Lohmann, J. Hendricks, and B. Kärcher, 2014: Dust ice nuclei effects on cirrus clouds. *Atmos. Chem. Phys.*, **14**, 3027–3046, https://doi.org/10.5194/acp-14-3027-2014.

Kupiszewski, P., and Coauthors, 2016: Ice residual properties in mixed-phase clouds at the high-alpine Jungfraujoch site. *J. Geophys. Res. Atmos.*, **121**, 12 343–12 362, https://doi.org/10.1002/2016JD024894.

Lee, D. S., and Coauthors, 2021: The contribution of global aviation to anthropogenic climate forcing for 2000 to 2018. *Atmos. Environ.*, **244**, 117834, https://doi.org/10.1016/j.atmosenv.2020.117834.

Lehmkuhl, F., H. Schüttrumpf, J. Schwarzbauer, C. Brüll, M. Dietze, P. Letmathe, C. Völker, and H. Hollert, 2022: Assessment of the 2021 summer flood in Central Europe. *Environ. Sci. Eur.*, **34**, 107, https://doi.org/10.1186/s12302-022-00685-1.

Lelli, L., M. Vountas, N. Khosravi, and J. P. Burrows, 2023: Satellite remote sensing of regional and seasonal Arctic cooling showing a multi-decadal trend towards brighter and more liquid clouds. *Atmos. Chem. Phys.*, **23**, 2579–2611, https://doi.org/10.5194/acp-23-2579-2023.

Li, Y., and Coauthors, 2023: Upper-tropospheric slightly ice-subsaturated regions: Frequency of occurrence and statistical evidence for the appearance of contrail cirrus. *Atmos. Chem. Phys.*, **23**, 2251–2271, https://doi.org/10.5194/acp-23-2251-2023.

Lucke, J. R., T. Jurkat, D. Baumgardner, F. Kalinka, M. Moser, E. De La Torre Castro, and C. Voigt, 2023: Characterization of atmospheric icing conditions during the HALO-(AC)^3 campaign with the Nevzorov probe and the backscatter cloud probe with polarization detection. *Int. Conf. on Icing of Aircraft, Engines, and Structures*, Vienna, Austria, 1224–1237, SAE International, https://doi.org/10.4271/2023-01-1485.

Luebke, A. E., and Coauthors, 2016: The origin of midlatitude ice clouds and the resulting influence on their microphysical properties. *Atmos. Chem. Phys.*, **16**, 5793–5809, https://doi.org/10.5194/acp-16-5793-2016.

——, A. Ehrlich, M. Schäfer, K. Wolf, and M. Wendisch, 2022: An assessment of macrophysical and microphysical cloud properties driving radiative forcing of shallow trade-wind clouds. *Atmos. Chem. Phys.*, **22**, 2727–2744, https://doi.org/10.5194/acp-22-2727-2022.

Mannstein, H., R. Meyer, and P. Wendling, 1999: Operational detection of contrails from NOAA-AVHRR-data. *Int. J. Remote Sens.*, **20**, 1641–1660, https://doi.org/10.1080/014311699212650.

Marjani, S., M. Tesche, P. Bräuer, O. Sourdeval, and J. Quaas, 2022: Satellite observations of the impact of individual aircraft on ice crystal number in thin cirrus clouds. *Geophys. Res. Lett.*, **49**, e2021GL096173, https://doi.org/10.1029/2021GL096173.

Märkl, R. S., and Coauthors, 2024: Powering aircraft with 100% sustainable aviation fuel reduces ice crystals in contrails. *Atmos. Chem. Phys.*, **24**, 3813–3837, https://doi.org/10.5194/acp-24-3813-2024.

Marsing, A., R. Meerkötter, R. Heller, S. Kaufmann, T. Jurkat-Witschas, M. Krämer, C. Rolf, and C. Voigt, 2023: Investigating the radiative effect of Arctic cirrus measured in situ during the winter 2015–2016. *Atmos. Chem. Phys.*, **23**, 587–609, https://doi.org/10.5194/acp-23-587-2023.

McFarquhar, G. M., and Coauthors, 2011: Indirect and semi-direct aerosol campaign: The impact of Arctic aerosols on clouds. *Bull. Amer. Meteor. Soc.*, **92**, 183–201, https://doi.org/10.1175/2010BAMS2935.1.

Mei, F., and Coauthors, 2020: Comparison of aircraft measurements during GoAmazon2014/5 and ACRIDICON-CHUVA. *Atmos. Meas. Tech.*, **13**, 661–684, https://doi.org/10.5194/amt-13-661-2020.

Mertens, M., A. Kerkweg, P. Jöckel, H. Tost, and C. Hofmann, 2016: The 1-way on-line coupled model system MECO(n)—Part 4: Chemical evaluation (based on MESSy v2.52). *Geosci. Model Dev.*, **9**, 3545–3567, https://doi.org/10.5194/gmd-9-3545-2016.

Mertes, S., B. Dippel, and A. Schwarzenböck, 2004: Quantification of graphitic carbon in atmospheric aerosol particles by Raman spectroscopy and first application for the determination of mass absorption efficiencies. *J. Aerosol Sci.*, **35**, 347–361, https://doi.org/10.1016/j.jaerosci.2003.10.002.

——, and Coauthors, 2007: Counterflow virtual impactor based collection of small ice particles in mixed-phase clouds for the physico-chemical characterization of tropospheric ice nuclei: Sampler description and first case study. *Aerosol Sci. Technol.*, **41**, 848–864, https://doi.org/10.1080/02786820701501881.

Meyer, J., and Coauthors, 2015: Two decades of water vapor measurements with the FISH fluorescence hygrometer: A review. *Atmos. Chem. Phys.*, **15**, 8521–8538, https://doi.org/10.5194/acp-15-8521-2015.

Minnis, P., J. K. Ayers, R. Palikonda, and D. Phan, 2004: Contrails, cirrus trends, and climate. *J. Climate*, **17**, 1671–1685, https://doi.org/10.1175/1520-0442(2004)017<1671:CCTAC>2.0.CO;2.

Murphy, D. M., D. S. Thomson, and M. J. Mahoney, 1998: In situ measurements of organics, meteoritic material, mercury, and other elements in aerosols at 5 to 19 kilometers. *Science*, **282**, 1664–1669, https://doi.org/10.1126/science.282.5394.1664.

Ng, J. Y.-H., and Coauthors, 2024: Contrail detection on GOES-16 ABI with the OpenContrails dataset. *IEEE Trans. Geosci. Remote Sens.*, **62**, 1–14, https://doi.org/10.1109/TGRS.2023.3345226.

Ogren, J. A., J. Heintzenberg, and R. J. Charlson, 1985: In-situ sampling of clouds with a droplet to aerosol converter. *Geophys. Res. Lett.*, **12**, 121–124, https://doi.org/10.1029/GL012i003p00121.

Ovarlez, J., J.-F. Gayet, K. Gierens, J. Ström, H. Ovarlez, F. Auriol, R. Busen, and U. Schumann, 2002: Water vapour measurements inside cirrus clouds in Northern and Southern hemispheres during INCA. *Geophys. Res. Lett.*, **29**, 1813, https://doi.org/10.1029/2001GL014440.

Patnaude, R., M. Diao, X. Liu, and S. Chu, 2021: Effects of thermodynamics, dynamics and aerosols on cirrus clouds based on in situ observations and NCAR CAM6. *Atmos. Chem. Phys.*, **21**, 1835–1859, https://doi.org/10.5194/acp-21-1835-2021.

Petters, M. D., and T. P. Wright, 2015: Revisiting ice nucleation from precipitation samples: ICE NUCLEATION from PRECIPITATION. *Geophys. Res. Lett.*, **42**, 8758–8766, https://doi.org/10.1002/2015GL065733.

Petzold, A., and Coauthors, 2017: Upper tropospheric water vapour and its interaction with cirrus clouds as seen from IAGOS long-term routine *in situ* observations. *Faraday Discuss.*, **200**, 229–249, https://doi.org/10.1039/c7fd00006e.

Pörtge, V., T. Kölling, A. Weber, L. Volkmer, C. Emde, T. Zinner, L. Forster, and B. Mayer, 2023: High-spatial-resolution retrieval of cloud droplet size distribution from polarized observations of the cloudbow. *Atmos. Meas. Tech.*, **16**, 645–667, https://doi.org/10.5194/amt-16-645-2023.

Rautenhaus, M., G. Bauer, and A. Dörnbrack, 2012: A web service based tool to plan atmospheric research flights. *Geosci. Model Dev.*, **5**, 55–71, https://doi.org/10.5194/gmd-5-55-2012.

——, M. Kern, A. Schäfler, and R. Westermann, 2015: Three-dimensional visualization of ensemble weather forecasts—Part 1: The visualization tool Met.3D (version 1.0). *Geosci. Model Dev.*, **8**, 2329–2353, https://doi.org/10.5194/gmd-8-2329-2015.

Righi, M., and Coauthors, 2020: Coupling aerosols to (cirrus) clouds in the global EMAC-MADE3 aerosol–climate model. *Geosci. Model Dev.*, **13**, 1635–1661, https://doi.org/10.5194/gmd-13-1635-2020.

——, J. Hendricks, and C. G. Beer, 2021: Exploring the uncertainties in the aviation soot–cirrus effect. *Atmos. Chem. Phys.*, **21**, 17 267–17 289, https://doi.org/10.5194/acp-21-17267-2021.

Rollins, A. W., and Coauthors, 2014: Evaluation of UT/LS hygrometer accuracy by intercomparison during the NASA MACPEX mission. *J. Geophys. Res. Atmos.*, **119**, 1915–1935, https://doi.org/10.1002/2013JD020817.

Sassen, K., 1997: Contrail-cirrus and their potential for regional climate change. *Bull. Amer. Meteor. Soc.*, **78**, 1885–1903, https://doi.org/10.1175/1520-0477(1997)078<1885:CCATPF>2.0.CO;2.

Schäfler, A., and M. Rautenhaus, 2023: Interactive 3D visual analysis of weather prediction data reveals midlatitude overshooting convection during the CIRRUS-HL field experiment. *Bull. Amer. Meteor. Soc.*, **104**, E1426–E1434, https://doi.org/10.1175/BAMS-D-22-0103.1.

——, and Coauthors, 2018: The North Atlantic waveguide and downstream impact experiment. *Bull. Amer. Meteor. Soc.*, **99**, 1607–1637, https://doi.org/10.1175/BAMS-D-17-0003.1.

Schiller, C., M. Krämer, A. Afchine, N. Spelten, and N. Sitnikov, 2008: Ice water content of Arctic, midlatitude, and tropical cirrus. *J. Geophys. Res.*, **113**, D24208, https://doi.org/10.1029/2008JD010342.

Schmale, J., P. Zieger, and A. M. L. Ekman, 2021: Aerosols in current and future Arctic climate. *Nat. Climate Change*, **11**, 95–105, https://doi.org/10.1038/s41558-020-00969-5.

Schnaiter, M., and Coauthors, 2016: Cloud chamber experiments on the origin of ice crystal complexity in cirrus clouds. *Atmos. Chem. Phys.*, **16**, 5091–5110, https://doi.org/10.5194/acp-16-5091-2016.

Schneider, J., and Coauthors, 2021: Aircraft-based observation of meteoric material in lower-stratospheric aerosol particles between 15 and 68°N. *Atmos. Chem. Phys.*, **21**, 989–1013, https://doi.org/10.5194/acp-21-989-2021.

Schumann, U., 2012: A contrail cirrus prediction model. *Geosci. Model Dev.*, **5**, 543–580, https://doi.org/10.5194/gmd-5-543-2012.

——, and H. Huntrieser, 2007: The global lightning-induced nitrogen oxides source. *Atmos. Chem. Phys.*, **7**, 3823–3907, https://doi.org/10.5194/acp-7-3823-2007.

——, J. E. Penner, Y. Chen, C. Zhou, and K. Graf, 2015: Dehydration effects from contrails in a coupled contrail–climate model. *Atmos. Chem. Phys.*, **15**, 11 179–11 199, https://doi.org/10.5194/acp-15-11179-2015.

——, L. Bugliaro, A. Dörnbrack, R. Baumann, and C. Voigt, 2021a: Aviation contrail cirrus and radiative forcing over Europe during 6 months of COVID-19. *Geophys. Res. Lett.*, **48**, e2021GL092771, https://doi.org/10.1029/2021GL092771.

——, and Coauthors, 2021b: Air traffic and contrail changes over Europe during COVID-19: A model study. *Atmos. Chem. Phys.*, **21**, 7429–7450, https://doi.org/10.5194/acp-21-7429-2021.

Seifert, M., J. Ström, R. Krejci, A. Minikin, A. Petzold, J.-F. Gayet, U. Schumann, and J. Ovarlez, 2003: In-situ observations of aerosol particles remaining from evaporated cirrus crystals: Comparing clean and polluted air masses. *Atmos. Chem. Phys.*, **3**, 1037–1049, https://doi.org/10.5194/acp-3-1037-2003.

Sprenger, M., and H. Wernli, 2015: The LAGRANTO Lagrangian analysis tool—Version 2.0. *Geosci. Model Dev.*, **8**, 2569–2586, https://doi.org/10.5194/gmd-8-2569-2015.

Strandgren, J., L. Bugliaro, F. Sehnke, and L. Schröder, 2017: Cirrus cloud retrieval with MSG/SEVIRI using artificial neural networks. *Atmos. Meas. Tech.*, **10**, 3547–3573, https://doi.org/10.5194/amt-10-3547-2017.

Teoh, R., U. Schumann, E. Gryspeerdt, M. Shapiro, J. Molloy, G. Koudis, C. Voigt, and M. E. J. Stettler, 2022a: Aviation contrail climate effects in the North Atlantic from 2016 to 2021. *Atmos. Chem. Phys.*, **22**, 10 919–10 935, https://doi.org/10.5194/acp-22-10919-2022.

——, and Coauthors, 2022b: Targeted use of sustainable aviation fuel to maximize climate benefits. *Environ. Sci. Technol.*, **56**, 17 246–17 255, https://doi.org/10.1021/acs.est.2c05781.

Tesche, M., P. Achtert, P. Glantz, and K. J. Noone, 2016: Aviation effects on already-existing cirrus clouds. *Nat. Commun.*, **7**, 12016, https://doi.org/10.1038/ncomms12016.

Thornberry, T. D., and Coauthors, 2013: Measurement of low-ppm mixing ratios of water vapor in the upper troposphere and lower stratosphere using chemical ionization mass spectrometry. *Atmos. Meas. Tech.*, **6**, 1461–1475, https://doi.org/10.5194/amt-6-1461-2013.

Tomsche, L., and Coauthors, 2022: Enhanced sulfur in the upper troposphere and lower stratosphere in spring 2020. *Atmos. Chem. Phys.*, **22**, 15 135–15 151, https://doi.org/10.5194/acp-22-15135-2022.

Unterstrasser, S., K. Gierens, I. Sölch, and M. Lainer, 2017: Numerical simulations of homogeneously nucleated natural cirrus and contrail-cirrus. Part 1: How different are they? *Meteor. Z.*, **26**, 621–642, https://doi.org/10.1127/metz/2016/0777.

Urbanek, B., S. Groß, M. Wirth, C. Rolf, M. Krämer, and C. Voigt, 2018: High depolarization ratios of naturally occurring cirrus clouds near air traffic regions over Europe. *Geophys. Res. Lett.*, **45**, 13 166–13 172, https://doi.org/10.1029/2018GL079345.

Vance, A. K., S. J. Abel, R. J. Cotton, and A. M. Woolley, 2015: Performance of WVSS-II hygrometers on the FAAM research aircraft. *Atmos. Meas. Tech.*, **8**, 1617–1625, https://doi.org/10.5194/amt-8-1617-2015.

Verma, P., and U. Burkhardt, 2022: Contrail formation within cirrus: Icon-LEM simulations of the impact of cirrus cloud properties on contrail formation. *Atmos. Chem. Phys.*, **22**, 8819–8842, https://doi.org/10.5194/acp-22-8819-2022.

Vochezer, P., E. Järvinen, R. Wagner, P. Kupiszewski, T. Leisner, and M. Schnaiter, 2016: In situ characterization of mixed phase clouds using the small ice detector and the particle phase discriminator. *Atmos. Meas. Tech.*, **9**, 159–177, https://doi.org/10.5194/amt-9-159-2016.

Voigt, C., and Coauthors, 2017: ML-CIRRUS: The airborne experiment on natural cirrus and contrail cirrus with the high-altitude long-range research aircraft HALO. *Bull. Amer. Meteor. Soc.*, **98**, 271–288, https://doi.org/10.1175/BAMS-D-15-00213.1.

——, and Coauthors, 2021: Cleaner burning aviation fuels can reduce contrail cloudiness. *Commun. Earth Environ.*, **2**, 114, https://doi.org/10.1038/s43247-021-00174-y.

——, and Coauthors, 2022: Cleaner skies during the COVID-19 lockdown. *Bull. Amer. Meteor. Soc.*, **103**, E1796–E1827, https://doi.org/10.1175/BAMS-D-21-0012.1.

Wang, Z., and Coauthors, 2023: Observations of microphysical properties and radiative effects of a contrail cirrus outbreak over the North Atlantic. *Atmos. Chem. Phys.*, **23**, 1941–1961, https://doi.org/10.5194/acp-23-1941-2023.

——, L. Bugliaro, K. Gierens, M. I. Hegglin, S. Rohs, A. Petzold, S. Kaufmann, and C. Voigt, 2025: Machine learning for improvement of upper-tropospheric relative humidity in ERA5 weather model data. *Atmos. Chem. Phys.*, **25**, 2845–2861, https://doi.org/10.5194/acp-25-2845-2025.

Weber, A., T. Kölling, V. Pörtge, A. Baumgartner, C. Rammeloo, T. Zinner, and B. Mayer, 2024: Polarization upgrade of specMACS: Calibration and characterization of the 2D RGB polarization-resolving cameras. *Atmos. Meas. Tech.*, **17**, 1419–1439, https://doi.org/10.5194/amt-17-1419-2024.

Wendisch, M., and Coauthors, 2005: Impact of cirrus crystal shape on solar spectral irradiance: A case study for subtropical cirrus. *J. Geophys. Res.*, **110**, D03202, https://doi.org/10.1029/2004JD005294.

——, P. Yang, and P. Pilewskie, 2007: Effects of ice crystal habit on thermal infrared radiative properties and forcing of cirrus. *J. Geophys. Res.*, **112**, D08201, https://doi.org/10.1029/2006JD007899.

——, and Coauthors, 2017: Understanding causes and effects of rapid warming in the Arctic. *Eos*, **98**, https://doi.org/10.1029/2017EO064803.

——, and Coauthors, 2023: Atmospheric and surface processes, and feedback mechanisms determining Arctic amplification: A review of first results and prospects of the $(AC)^3$ project. *Bull. Amer. Meteor. Soc.*, **104**, E208–E242, https://doi.org/10.1175/BAMS-D-21-0218.1.

Wernli, H., and H. C. Davies, 1997: A Lagrangian-based analysis of extratropical cyclones. I: The method and some applications. *Quart. J. Roy. Meteor. Soc.*, **123**, 467–489, https://doi.org/10.1256/smsqj.53810.

——, M. Boettcher, H. Joos, A. K. Miltenberger, and P. Spichtinger, 2016: A trajectory-based classification of ERA-Interim ice clouds in the region of the North Atlantic storm track. *Geophys. Res. Lett.*, **43**, 6657–6664, https://doi.org/10.1002/2016GL068922.

Wirth, M., A. Fix, P. Mahnke, H. Schwarzer, F. Schrandt, and G. Ehret, 2009: The airborne multi-wavelength water vapor differential absorption lidar WALES: System design and performance. *Appl. Phys.*, **96B**, 201–213, https://doi.org/10.1007/s00340-009-3365-7.

Wolf, K., A. Ehrlich, M. Jacob, S. Crewell, M. Wirth, and M. Wendisch, 2019: Improvement of airborne retrievals of cloud droplet number concentration of trade wind cumulus using a synergetic approach. *Atmos. Meas. Tech.*, **12**, 1635–1658, https://doi.org/10.5194/amt-12-1635-2019.

Xu, G., M. Schnaiter, and E. Järvinen, 2022: Accurate retrieval of asymmetry parameter for large and complex ice crystals from in-situ polar nephelometer measurements. *J. Geophys. Res. Atmos.*, **127**, e2021JD036071, https://doi.org/10.1029/2021JD036071.

Zahn, A., J. Weppner, H. Widmann, K. Schlote-Holubek, B. Burger, T. Kuhner, and H. Franke, 2012: A fast and precise chemiluminescence ozone detector for eddy flux and airborne application. *Atmos. Meas. Tech.*, **5**, 363–375, https://doi.org/10.5194/amt-5-363-2012.

——, and Coauthors, 2024: IAGOS-CARIBIC MS files collection (v2024.01.12). Zenodo, accessed 28 October 2024, https://doi.org/10.5281/zenodo.10495597.

Zelinka, M. D., T. A. Myers, D. T. McCoy, S. Po-Chedley, P. M. Caldwell, P. Ceppi, S. A. Klein, and K. E. Taylor, 2020: Causes of higher climate sensitivity in CMIP6 models. *Geophys. Res. Lett.*, **47**, e2019GL085782, https://doi.org/10.1029/2019GL085782.

Zieger, P., D. Heslin-Rees, L. Karlsson, M. Koike, R. Modini, and R. Krejci, 2023: Black carbon scavenging by low-level Arctic clouds. *Nat. Commun.*, **14**, 5488, https://doi.org/10.1038/s41467-023-41221-w.

Ziereis, H., and Coauthors, 2022: Redistribution of total reactive nitrogen in the lowermost Arctic stratosphere during the cold winter 2015/2016. *Atmos. Chem. Phys.*, **22**, 3631–3654, https://doi.org/10.5194/acp-22-3631-2022.